Development and Optimization of a Multifunctional Sensor for Measuring Soil Thermal Properties, Water Retention Characteristics and Electrical Conductivity

Jiagui Hou[1], Yaohui Cai[2], Chaoyue Zhao[1], Junru Chen[1], Lang Jia[1], Zuyao Chen[1], Francis Zvomuya[3], Hailong He[1, *]

[1] College of Natural Resources and Environment, Northwest A&F University, Yangling, Shaanxi 712100, China (jiagui.hou@nwafu.edu.cn; zhzcyue@nwafu.edu.cn; junru.chen@nwafu.edu.cn; jialang@nwafu.edu.cn; zyao_chen@163.com; hailong.he@hotmail.com)

[2] College of Soil and Water Conservation Science and Engineering, Northwest A&F University, Yangling, Shaanxi 712100, China (caiyh@nwafu.edu.cn)

[3] Department of Soil Science, University of Manitoba, Winnipeg, Manitoba R3T 2N2, Canada (francis.zvomuya@umanitoba.ca)

Correspondence: hailong.he@hotmail.com (H.H.)

Highlights

- By coupling porous ceramic matrix to heat pulse and time domain reflectometry, a multifunctional sensor which can simultaneously measure soil thermal properties, water retention characteristics and electrical conductivity was developed
- COMSOL simulations were used to optimize sensor dimension and verified with experimental measurements
- Considering the different combinations of porous ceramic matrix and soil water content, the measurement errors of soil thermal conductivity (288 treatments) and porous ceramic matrix thermal conductivity (including the

errors caused by radial heat conduction and axial heat conduction, 288 treatments respectively), dielectric permittivity (3960 treatments) and electrical conductivity (5940 treatments) were evaluated

- Porous ceramic matrix radius of 18 mm, ceramic length of 40 mm and extended rod length of 50 mm is the optimal sensor design

Abstract:

Soil water content, matric potential, thermal properties, and electrical conductivity are fundamental and interrelated properties required by a variety of applications in soil science, hydrology, agriculture, and engineering. However, the measurements of the properties are affected by the temporal and spatial variability of soil due to employment of a variety of sensors, which hinders the research and modeling of coupled water, heat and solute transport. In addition, the laborious, costly and time-consuming sensor optimization is always a challenge for traditional sensor development. The objective of this study was to develop a multifunctional sensor integrating heat pulse, time domain reflectometry and porous ceramic matrix and optimize the sensor with COMSOL based numerical simulations. COMSOL simulated ceramic properties (e.g., thermal conductivity, volumetric heat capacity, dielectric permittivity, electrical conductivity) and soil properties (e.g., thermal conductivity and volumetric heat capacity) with different scenarios of sensor dimensions (e.g., the radius and length of the ceramic and extended rod length) were systematically evaluated and verified with experimental data. Our results show that the optimal radius and length of the ceramic are 18 mm and 40 mm, respectively, and the optimal rod length extended out of the ceramic is 50 mm. The optimized results indicate low estimation errors for dielectric permittivity (±1%), electrical conductivity (±1%), thermal conductivity (±2%), and volumetric heat capacity (±1%) of the ceramic as well as thermal conductivity (±3%) and volumetric heat capacity (±1%) of soil. The new multifunctional sensor can provide accurate measurement and modeling of soil hydrothermal properties.

Keywords: Thermo-TDR, thermal/heat dissipation, matric potential, heterogeneity, measurement sensitivity, finite element simulation

Abbreviations: AC/DC, alternating current/direct current; DPHP, dual-probe heat pulse; Ho, homogeneous soil without ceramic; I, rods subjected to inward deflection; ILS, infinite line source; M, measured data; *MSC*, measurement sensitivity to the

ceramic; *MSS*, measurement sensitivity to the soil; N, rods subjected to no deflection; O, rods subjected to outward deflection; RE_a, absolute value of relative error; *RMSE*, root means square error; S, simulated data; STP, soil thermal properties; SWRC, soil water retention characteristics; TDR, time domain reflectometry; Thermo-TDR, heat pulse-time domain reflectometry.

1 Introduction

Soil thermal properties (STP) and soil water retention characteristics (SWRC) determining the soil thermal dynamics, status and momentum of water (e.g., ice, liquid water or vapor), affecting a series of processes such as crop growth and development (Nagai and Makino 2009), soil structure change (Zhang et al. 2017), water and energy exchange between land and atmosphere (Brocca et al. 2013), and distribution of solute, gas, water and energy in soil (Mortensen et al. 2006). They are therefore closely related to hydrological, meteorological, agricultural, engineering, ecological environment and geophysical research (Saito et al. 2006). Among them, SWRC represents the relationship between water content (θ, cm^3 cm^{-3}) and matric potential (ψ_m, kpa), and STP are important parameters for evaluating surface energy and geothermal resources, which mainly include thermal conductivity (λ, W m^{-1} $°C^{-1}$), volumetric heat capacity (C, M J m^{-3} $°C^{-1}$), and thermal diffusivity (κ, m^2 s^{-1}). Accurate, non-destructive, continuous and simultaneous monitoring of these properties at both laboratory and field is therefore of great significance, especially with the development of smart agriculture and hydrology (Lekshmi et al. 2014; Bwambale et al. 2022; Datta and Taghvaeian 2023).

A variety of techniques for measuring SWRC and STP have been developed. For instance, the dual-probe heat pulse (DPHP) method (He et al. 2018), time domain reflectometry (TDR) method (Robinson et al. 2003; He et al. 2021; He et al. 2023), and ceramics or gypsum based matric potential sensors are currently the most widely used techniques to continuously, rapidly and accurately measure STP, θ and electrical conductivity (EC, σ), and ψ_m, respectively in both laboratory and field. These methods share similarities in measuring principles. For example, DPHP estimate STP based on transport of heat by solving the heat transport equation and TDR measure soil water content based on the dielectric permittivity of water that is much greater than other soil components (e.g., 80 for water vs 5–10 for other components at room

90 temperature). Existing matric potential sensors estimate soil matric potential by
91 indirectly measuring change of soil water content (Noborio et al. 1996; Or and Wraith
92 1999), thermal conductivity or heat capacity (Phene et al. 1971; Reece 1996; Kojima
93 et al. 2017; Kojima et al. 2021), or electrical resistance or conductivity (Xin et al.
94 2007) of a porous ceramic or gypsum matrix in equilibrium with its surrounding soils.
95 However, employment of the abovementioned DPHP, TDR and matric potential
96 sensors is affected by unmatched measurement frequency, sensing volume and
97 installation locations between the sensors due to the highly temporal and spatial
98 variability of the soil. This is among the dominant challenges for coupled water and
99 heat transport.

100 Previous studies have attempted to combine these methods for measuring
101 multiple soil properties with satisfactory performance. For instance, coiled TDR
102 (Noborio et al. 1999; Scanlon et al. 2002; Lungal and Si 2008) or time domain
103 transmissometry (Kojima et al. 2023) was incorporated into ceramics or gypsum to
104 simultaneously measure both water content and matric potential to obtain the SWRC,
105 which describes the change of water content as a function of matric potential. Ren et
106 al. (1999) combined DPHP and time domain reflectometry to develop the thermo-
107 TDR or T-TDR technique for continuous and simultaneous measurement of θ, σ,
108 temperature (T), C, λ and κ of the same soil sample. However, thermo-TDR cannot
109 measure ψ_m that is needed to study soil water movement and the short TDR needs to
110 be calibrated for accurate estimate of θ (He et al. 2015; He et al. 2018). Kojima et al.
111 (2021) incorporated part of DPHP sensor into a ceramic block to simultaneously
112 estimate θ, C, and λ (by DPHP) as well as ψ_m (by ceramics) of the same soil sample.
113 However, it indirectly estimates soil water content with additional known information
114 (e.g., bulk density, ρ_b) and would introduce extra uncertainties in measurement
115 without calibrations and limits its application in the field to continuously monitor θ
116 (Ren et al. 2005). Moreover, a soil multifunctional sensor coupling TDR can be used
117 to measure EC (Dalton et al. 1984; Kargas and Soulis 2019; He et al. 2021). Currently

there is an urgent need for a multifunctional sensor that enables the fully couple of DPHP, TDR and porous ceramic matrix for simultaneous measurement of STP and SWRC.

A good design is imperative to the high accuracy of the multifunctional sensor. According to the infinite line heat source (ILS) model, the heater size of DPHP is usually simplified, that is, the heat source of finite length is considered as the heat source of infinite length, and the cylindrical heat source is considered as the linear heat source (Campbell et al. 1991; Bristow et al. 1994). The rod of the DPHP should be slender to conform to the ILS model. However, the design results in a variable rod spacing (r, mm), which increases the measurement error of C (Noborio et al. 1996). A small r allows easier identification of the maximum temperature rise and the time corresponding to the maximum temperature rise at a lower heat strength (q', W m^{-1}), effectively avoiding convective heat transfer around the heater. However, a small r means a higher relative error in determining r and less representative measurements, because of the small sampling volume (Ren et al. 1999). Therefore, the DPHP was designed with a rod length (L) of 28 mm, a rod diameter (d) of 0.8 mm, and an r of 6 mm (Bristow et al. 1994). To reduce the TDR signal attenuation (which varies with soil texture, θ, and σ) and accurately estimate the travel time, the maximum and minimum rod lengths of the TDR rod can be estimated as (Dalton and Van Genuchten 1986; Ren et al. 1999):

$$L_{max} = \frac{\ln\left(\frac{V_T}{V_R}\right) \cdot \sqrt{\varepsilon}}{12\pi\sigma} \quad (1)$$

$$L_{min} = \frac{t_e v_0}{2\sqrt{\varepsilon}} \quad (2)$$

where L_{max} and L_{min} are the maximum and minimum rod lengths (m), respectively, V_T and V_R are excitation voltage and reflected voltage (V), respectively, ε is dielectric permittivity, σ is electrical conductivity (dS m^{-1}), t_e is the travel time of electromagnetic wave (s), and v_0 is the velocity of light in a vacuum (3×10^8 m s^{-1}).

To avoid the skin effect and excessive soil disturbance, the ratio of rod spacing to rod diameter (r/d) should be as large as possible but less than 10 (Knight 1992). Considering the accuracy of soil thermal properties and water content measurement, the thermo-TDR developed by Ren et al. (1999) was designed with a L of 40 mm, d of 1.3 mm, and r of 6 mm.

In addition, traditional sensor optimization requires numerous designs/types (e.g., sensor dimension: rod length and size, rod spacing, material, and heat strategies) for comparison and screening the best-performing sensor design (Or and Wraith 1999; Liu et al. 2008; Kamai et al. 2015; Menne et al. 2022). This approach is effective but costly, time consuming and laborious, the best optimized design may not be properly selected and the sampling volume and interferences among methods may still remain unknown. Therefore, there is a need to introduce numerical simulations to facilitate probe design in order to comprehensively evaluate numerous factors and their combinations affecting the sensor, and avoid the effects of uncontrollable sources of error in applications (Zhao et al. 2023). A few previous studies have analyzed various factors affecting the accuracy of TDR or DPHP based on numerical simulation software such as GeoStudio (Zhan et al. 2015), HYDRUS (Saito et al. 2007), and COMSOL (Rakesh et al. 2021; Meng et al. 2023). This approach has been approved effectively and cost effective and led to improvements in sensor design and construction under different measurement conditions, which in turn improved the measurement range, accuracy and precision of newly designed sensors. Numerical simulations have the potential to optimize multifunctional sensors combing the DPHP, TDR and ceramics.

Therefore, the objective of this study was to design a soil multifunctional sensor and optimize it using numerical simulation. DPHP, TDR and matric potential sensor were coupled to allow the simultaneous and continuous measurement of SWRC and STP of the same soil, that is, to obtain unified soil hydrothermal data in the same time and space. COMSOL that supports multi-physical field simulations was used to

quantitatively analyze the measurement error and to optimize sensor design in terms of soil-ceramic equilibrium as well as heat (for heat pulse measurements) and electromagnetic transfer (for TDR measurements).

2 Materials and methods

2.1 Porotype sensor development

We developed a soil multifunctional sensor by coupling a porous ceramic matrix to extended thermo-TDR rods (**Figure 1**). The ceramic was prepared by a sintering technology, with raw materials of diatomite, kaolin, dextrin, activated carbon powder and silica sol at a mass ratio of 8: 3: 2: 7: 9. The raw materials were mixed, filled into a specific mold, and pressed at a pressure of 12 Mpa for 3 min. It was sintered in a muffle furnace at 1200 ℃ for 15 h after drying at room temperature for 24 h. The activated carbon powder was composed of equal weights of five different particle sizes (< 75 μm, 75–250 μm, 125–250 μm, 250–400 μm, and 400–1000 μm) of powder. The activated carbon power was used as a pore-forming agent, which sublimated during sintering, forming numerous pores of different sizes. A ceramic with wide pore size distribution can prevent hydraulic decoupling due to a mismatch between the pore size distribution of the sensor and that of the soil, thus providing maximum sensitivity in the range of matric potential studied (Phene et al. 1971; Malazian et al. 2011; Menne et al. 2022). The thermo-TDR in this study was a traditional three-rod sensor, with rod spacing r of 6 mm and rod diameter d of 1.3 mm. The heating wires were placed in the middle rod as a linear heat source. Two thermocouples were placed in each rod to sense the temperature rise of the ceramic and soil. High-thermal-conductivity epoxy glue was then drawn into hollow place next to heating wires and thermocouples in the rods to construct a water-resistant, electrically-insulated rod. The joints of the electrical leads and the heating wires or the thermocouples were soldered. For the TDR part of the sensor, the central rod and two external rods were connected to the positive central lead and metal shield of the

coaxial cable, respectively. The joints of the rods and the electrical leads were then encased in epoxy as the sensor handle.

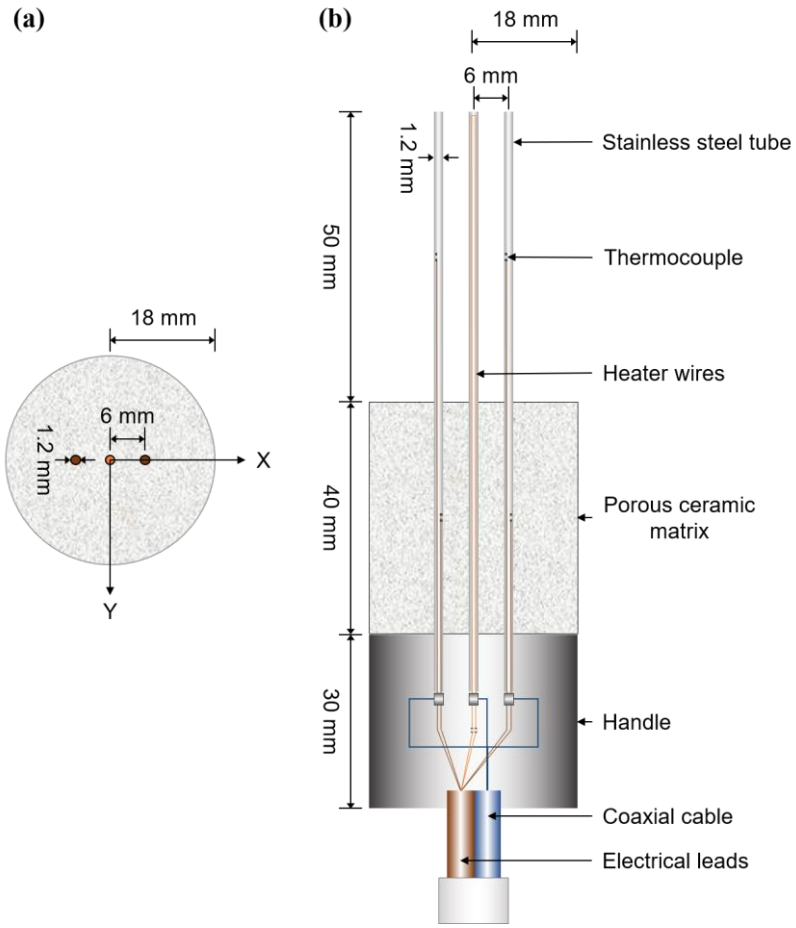

Figure 1. Front view (a) and cross section view (b) of the soil multifunctional sensor.

The rod base of the sensor was incorporated into a ceramic (**Figure 1**). The extended rods were in contact with the soil to directly measure soil water content and thermal properties when the sensor is placed in the soil. The base rods were in contact with the ceramic to measure ceramic thermal properties, water content and electrical conductivity. The ceramic matric potential was estimated using the pre-determined calibration curve (λ-ψ_m, C-ψ_m, θ-ψ_m or σ-ψ_m). Depending on different measurement environments, the various calibration curves proposed in this study can be selected to achieve the highest prediction accuracy of matric potential. The measured ceramic matric potential was equal to the soil matric potential when both of them are at

212 equilibrium.

213 The following two sections focus on the sensor optimization in terms of soil-
214 ceramic equilibrium and meanwhile considering the effects of heat transfer for DPHP
215 measurements (**Section 2.2**) and electromagnetic transport for TDR measurements
216 (**Section 2.3**) with COMSOL simulations. Different scenarios were tested and
217 literature data were used for verification and validation.

218 **2.2 COMSOL simulation of heat transport with heat pulse method**

219 **2.2.1. Numerical model setup and governing equations**

220 An optimal ceramic should be small to ensure faster water equilibration and
221 prevent excessive soil disturbance. However, a too small ceramic radius (R_C, mm)
222 leads to heat loss from the ceramic in the radial direction, and a too short ceramic
223 length (L_C, mm) leads to the measured temperature rise released by the heat pulse
224 method being affected by the axial heat transfer at the interface between the two
225 mediums. A 2D axisymmetric model of module of heat transfer in solids in COMSOL
226 (Version 6.1, COMSOL, Inc., Burlington, MA, USA) was used to optimize the sensor
227 size based on the module of heat transfer in solids. The governing equation used in the
228 module is:

229 $$C\frac{\partial T}{\partial t} = \nabla \cdot (\lambda \nabla T) + Q \quad t > 0 \tag{3}$$

230 where t is time (s), Q is rate per unit volume of heat generation for the numerical
231 model (W m^{-3}). Assuming that the heat is uniformly distributed in the heater of heat
232 pulse, then in the heater volume, Q can be represented by:

233 $$Q = \begin{cases} q'/S_H & 0 < t \le t_0 \\ 0 & t > t_0 \end{cases} \tag{4}$$

234 where S_H is the cross-sectional area of the heater (m^2), t_0 is the heat pulse duration (s).
235 For a linear heat source, d is negligible, i.e., S_H approaches 0.

236 As shown in **Figure 2a**, soil, ceramic and handle were represented by rectangles
237 with dimensions of 80 mm width × 200 mm height, 30 mm width × 65 mm height and

30 mm width × 65 mm height, respectively. Note that L_C and R_C could be modified in subsequent tests. To simplify the model, the heater and the temperature-sensing rods were not shown in the figure. A linear heat source was added on the axis of symmetry. The linear heat source was 140 mm in length, of which 10 mm was in the lower end of the handle, 65 mm was distributed throughout the ceramic and the remaining 65 mm was in the soil. The length of the heat source in the ceramic and the soil could be modified with the L_C and the length of the extended rod buried in soil (L_S, mm) in the subsequent simulation. The distance between the domain point probe and the linear heat source was 6 mm, corresponding to the rod spacing of 6 mm. The temperature rise curves of the ceramic and the soil were obtained using domain point probes. The outer boundary of the entire study region was set to thermal insulation. This boundary condition indicates that the heat flowing across the outer boundary is negligible. This setting is reasonable because a sufficiently large area is chosen for analysis to conform to the assumption of the infinite measured medium in the ILS model. The material properties of the handle were set to λ = 0.36 W m^{-1} °C^{-1}; density, ρ = 1410 kg m^{-3}; and specific heat, c = 1286 J kg^{-1} °C^{-1} (Kamai and Hopmans 2007). The setup of material properties for ceramic and soil are described in detail in **Section 2.2.3**. Since the mesh resolution affects simulation accuracy, we established a maximum mesh size of 0.92 mm in the ceramic region and the region between the heater and the temperature-sensing rod. The maximum mesh size for the other regions increased from 0.92 mm to 2.3 mm based on a maximum element growth rate of 1.1 (**Figure 2a**). To generate easier identification of the maximum temperature rise and avoid convective heat transfer around the heater, Kluitenberg (2002) suggested maximum temperature rise should fall in the range of 0.5–1.5 °C. Based on this, by testing the ceramic and soil with different water content, the optimal q' and t_0 were determined to be 58 W m^{-1} and 8 s, respectively.

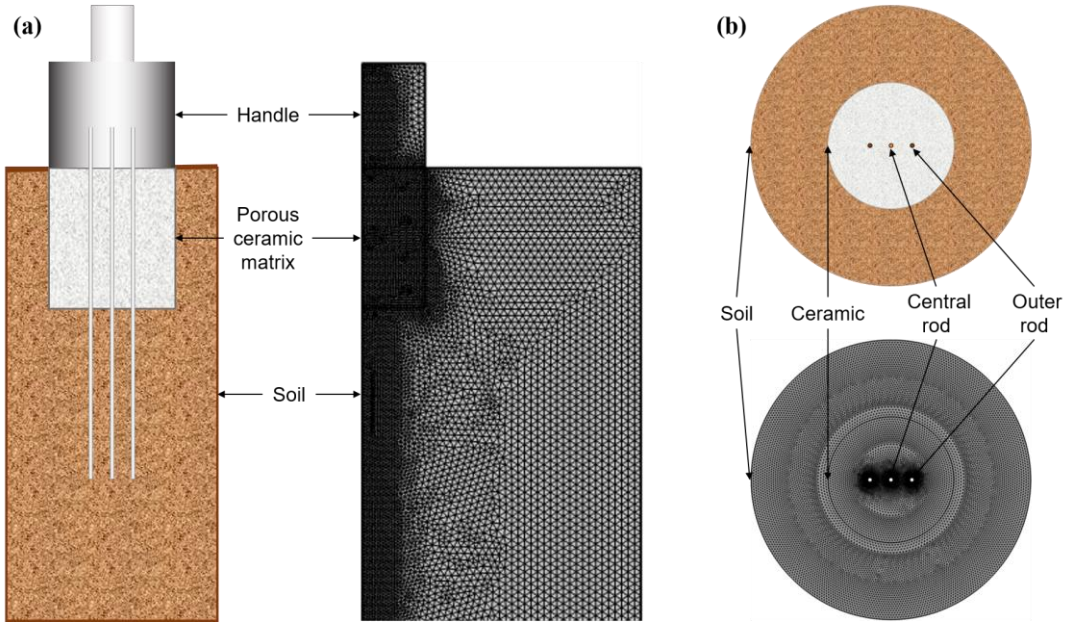

Figure 2. The scenario and the mesh for (a) heat pulse numerical simulation (the mesh area was not completely drawn) and (b) TDR sensitivity simulation.

2.2.2. Verification of heat pulse simulation

The validity of heat pulse simulation were verified based on the experimental setup and measured data of Mori et al. (2003) and Kluitenberg et al. (2010). The thermal properties of dry sand, water and saturated sand measured by heat pulse were simulated by adjusting the sensor setup and the material properties of the measured medium. In Kluitenberg et al. (2010), the L of the sensor was 27 mm, and the r was 4.99, 5.81 and 6.66 mm, corresponding to the rods subjected to inward deflection, no deflection, and outward deflection, respectively. Applied q' was 110 W m^{-1} for t_0 of 8 s. The λ, ρ and specific heat c of the measured medium are shown in **Table 1**.

Table 1. *Material properties for simulation verification. Note that the symbol λ represents thermal conductivity, ρ represents wet bulk density, and c represents specific heat.*

Medium	Deflection treatment	λ (W m^{-1} °C^{-1})	ρ (kg m^{-3})	c (J kg^{-1} °C^{-1})
Dry sand	inward	0.26	1630	759
	none	0.26	1630	759
	outward	0.29	1630	759
Water	inward	0.6	998	4182
	none	0.6	998	4182
	outward	0.59	998	4182

	inward	1.85	2000	1393
Saturated sand	none	1.85	2000	1393
	outward	1.89	2000	1393

2.2.3. Material properties for heat pulse simulations

Measurement using the multifunctional sensor requires that water in ceramic equilibrates with soil water, but this does not mean that the water contents of the two mediums are equal, and the water content gradient may change due to the surrounding soil. To broaden the applicability of the simulation, 36 water content combinations were considered, i.e., six degrees of saturation ranging from dry to saturation (the water content at saturation is equal to total porosity) were set to ceramic and soil, respectively. The degrees of saturation or water contents of the medium was numerically reflected by λ, c and ρ. The thermal conductivity and specific heat of ceramic corresponding to different water contents were measured by a thermo-TDR and the wet bulk density of ceramic was measured by weighing. The sandy soil provided by Kodešová et al. (2013), which had a wide range of thermal conductivity, was used as the simulated soil. The sandy soil comprised of 93.7% sand, 3% silt, and 3.3% clay, with ρ = 1710 kg m^{-3}, porosity (p) of 0.396 and volumetric heat capacity of solids ($\rho_{solids}c_{solids}$), of 2.164 M J m ^{3} °C^{-1}.

The thermal conductivity corresponding to different soil water contents was predicted based on the Yan et al. (2019) model:

$$\lambda = \begin{cases} \lambda_{dry} & \theta \le 0.01 \\ \left(\lambda_{sat} - \lambda_{dry}\right)\dfrac{1+\left(\dfrac{p}{\beta}\right)^{-\beta}}{1+\left(\dfrac{\theta}{\beta}\right)^{-\beta}} + \lambda_{dry} & \theta > 0.01 \end{cases} \quad (5)$$

where λ_{dry} and λ_{sat} are dry and saturated thermal conductivity, respectively (W m^{-1} °C^{-1}); β is empirical parameter; λ_{dry} was calculated by the linear function proposed by He et al. (2017):

$$\lambda_{dry} = -0.5815p + 0.4999 \quad p \le 0.86 \quad (6)$$

λ_{sat} was calculated by the geometric mean model proposed by Woodside and

Messmer (1961):

$$\lambda_{sat} = \lambda_w^{p} \lambda_{solids}^{1-p} \quad (7)$$

where λ_w is the thermal conductivity of water, which is 0.594 W m^{-1} °C^{-1} at 20 °C (Bristow 2002), λ_{solids} is the thermal conductivity of solids, which can be determined by another geometric mean model based on the thermal conductivity and mass fractions of quartz and other minerals (Johansen 1975; He et al. 2020):

$$\lambda_{solids} = \lambda_q^{qc} \lambda_o^{1-qc} \quad (8)$$

where qc is quartz content, λ_q is thermal conductivity of quartz (7.7 W m^{-1} °C^{-1}), and λ_o is thermal conductivity of other minerals, which is assumed to be 2.0 W m^{-1} °C^{-1} and 3.0 W m^{-1} °C^{-1} for soils with qc > 20% and qc ≤ 20%, respectively. Similar to Peters-Lidard et al. (1998), Lu et al. (2007) and He et al. (2020), quartz content was assumed to be equal to the sand content. According to Yan et al. (2019), β was calculated based on the sand fraction for soil solids (f_{sa}, gravimetric %):

$$\beta = -0.303\lambda_{sat} - 0.201 f_{sa} + 1.532 \quad (9)$$

And the ρ of the soil was predicted based on ρ_b and θ, written as:

$$\rho = \rho_b + \theta\rho_w \quad (10)$$

where ρ_w is the density of water (1000 kg m^{-3}). The c of the soil was calculated as:

$$c = C / \rho \quad (11)$$

where the C of soil was predicted from the volumetric heat capacity of soil solids and water:

$$C = (1-p)\rho_{solids} c_{solids} + \theta\rho_w c_w \quad (12)$$

where c_w is the specific heat of water (4180 J kg^{-1} °C^{-1}). The soil physical properties corresponding to saturation degrees (i.e., ratio of water content to saturated water content) of 0, 0.2, 0.4, 0.6, 0.8, 1.0 were used. The material properties of ceramic and soil are shown in **Table 2**.

The effect of R_C, L_C and L_S on the measurements were studied by changing the basic sensor dimension in **Section 2.1**. Only one effect was assessed in each

simulation to avoid complications from additional effects. The ceramic temperature rise with 8 R_C gradients (9, 12, 15, 18, 21, 24, 27 and 30 mm) and 36 water content combinations (288 treatments) was simulated. Ceramic thermal conductivity (λ_C) was estimated based on the pulsed infinite line source model, which was used to screen the optimal R_C. The optimal R_C was used to optimize L_C, with the L_C set to 30, 35, 40, 45, 50, 55, 60 and 65 mm. Similarly, the optimization results were used to optimize L_S, and the settings of L_S and L_C were consistent.

Table 2. *Material properties of the ceramic and soil for simulations. Note that the symbol λ represents thermal conductivity, ρ represents wet bulk density*, and *c represents specific heat.*

Medium	λ (W m^{-1} °C^{-1})	ρ (kg m^{-3})	c (J kg^{-1} °C^{-1})
Dry ceramic	0.35	951	1049
Unsaturation ceramic 1	0.53	1071	1472
Unsaturation ceramic 2	0.61	1192	1668
Unsaturation ceramic 3	0.74	1278	1802
Unsaturation ceramic 4	0.95	1311	2037
Saturation ceramic	1.37	1427	2093
Dry soil	0.27	1710	764
Unsaturation soil l	1.63	1789	916
Unsaturation soil 2	2.04	1868	1054
Unsaturation soil 3	2.30	1948	1181
Unsaturation soil 4	2.50	2027	1298
Saturation soil	2.65	2106	1407

2.3 COMSOL simulations of TDR-measured dielectric permittivity and electrical conductivity

2.3.1. Theory for measurement sensitivity of TDR

Ignoring the effect on the measurements of the heterogeneity of dielectric permittivity in the plane parallel to the rods, the effective dielectric permittivity (ε_{eff}) and effective electrical conductivity (σ_{eff}) can be predicted by the sensitivity of TDR rods to lateral variations in dielectric permittivity (Knight 1992; Ferré et al. 2003; Nissen et al. 2003). The spatial weighting factor $w(x, y)$ is the energy proportion of a specific point in the heterogeneous medium field with the same boundary conditions.

346 The $w(x, y)$ at each point for the spatial sensitivity of the TDR rod is defined as:

347 $$w(x,y) = \frac{\left|\nabla\Phi(x,y)\right|^2}{\iint_\Omega \left|\nabla\Phi_0(x,y)\right|^2 dxdy} \quad (13)$$

348 where $\nabla\Phi(x, y)$ and $\nabla\Phi_0(x, y)$ are potential gradients in homogeneous and
349 heterogeneous fields (V m^{-1}), respectively. The $\nabla\Phi(x, y)$ satisfies:

350 $$\nabla\Phi(x,y) = -E(x,y) \quad (14)$$

351 where $E(x, y)$ is the electric field intensity (V m^{-1}) and could be computed using
352 COMSOL. The weighting function is defined as:

353 $$\iint_\Omega w(x,y)dxdy = 1 \quad (15)$$

354 ε_{eff} and σ_{eff} are calculated as:

355 $$\varepsilon_{eff} = \iint_\Omega \varepsilon(x,y)w(x,y)dxdy \quad (16)$$

356 $$\sigma_{eff} = \iint_\Omega \sigma(x,y)w(x,y)dxdy \quad (17)$$

357 The contribution level of the measured medium (ceramic) to ε_{eff} is expressed as the
358 measurement sensitivity to the ceramic of the TDR (*MSC*):

359 $$MSC = \iint_C w_C(x,y)dxdy \quad (18)$$

360 where $w_C(x, y)$ is the weighting factor that is distributed in the ceramic region.
361 Similarly, the measurement sensitivity to the soil surrounding the ceramic of the TDR
362 (*MSS*) is:

363 $$MSS = \iint_S w_S(x,y)dxdy \quad (19)$$

364 where $w_S(x, y)$ is the weighting factor that is distributed in the soil region. In a plane
365 perpendicular to the TDR rods, *MST* and *MMS* satisfy:

366 $$MSC + MSS = 1 \quad (20)$$

367 The effective ceramic dielectric permittivity ($\varepsilon_{eff\text{-}C}$) and effective ceramic electrical
368 conductivity ($\sigma_{eff\text{-}C}$) measured by TDR can be expressed as:

369 $$\varepsilon_{eff\text{-}C} = MSC \times \varepsilon_C + MSS \times \varepsilon_S \quad (21)$$

370 $$\sigma_{eff\text{-}C} = MSC \times \sigma_C + MSS \times \sigma_S \quad (22)$$

where ε_C and ε_S are the apparent dielectric permittivity of ceramic and soil, respectively, and σ_C, σ_S, are the apparent electrical conductivity of ceramic and soil, respectively. Therefore, a greater value of the *MSC* for TDR indicates a larger sensitivity to the ceramic and a higher accuracy.

2.3.2. Simulation setup in the module of alternating current/direct current

The ceramic radius in terms of electromagnetic propagation was optimized by using the alternating current/direct current (AC/DC) module of COMSOL. A 2D model was established to simulate the electrostatic field perpendicular to the plane of the TDR rods. As shown in **Figure 2b**, the central rod of the TDR, ceramic and soil surrounding ceramic were represented by circles with radii of 0.6, 7 (adjustable) and 40 mm, respectively. At 6 mm to the left and to the right of the central rod, two circles with a radius of 0.6 mm were added to represent the outer rods. The entities of the three smallest circles are subtracted to simplify the model. The initial value of the entire study region was set to 0. Similar to Bruvik et al. (2012) and Zhan et al. (2015), the outer boundary of the soil and the two outer rods was set as zero charge and ground boundary conditions, respectively, and the central rod was set as terminal boundary condition, with the type voltage and the value of 1. Different combinations of ceramic radius and dielectric permittivity were set by parametric sweep to yield different electrostatic fields. The ceramic dielectric permittivity was set to 3, 6, 9, 12, 15, and 19, as measured by a TDR. The ceramic dielectric permittivity was set to 2, 5, 10, 15, 20, and 25, corresponding to the soil water content from drying to saturation (Nissen et al. 2003; Lekshmi et al. 2014). The ceramic radius increased from 7 to 18 mm in steps of 0.1 mm. Therefore, 3960 (6 × 6 × 110) treatments were set. The mesh used was the smallest mesh by default (0.0016–0.8 mm).

The matric potential sensor based on the relationship between the ressistance and matric potential fails when the electrical conductivity is higher than 0.5 dS m^{-1} (Campbell and Gee 1986; Xin et al. 2007). Therefore, the electrical conductivity set in this study ranged from 0.01 to 0.50 dS m^{-1}. In addition, the electrical conductivity is

related to the water content, that is, there is a certain correlation between the electrical conductivity and the dielectric permittivity (Hamed et al. 2003; Kargas and Soulis 2019). Consequently, 54 electrical conductivity combinations based on low, medium and high water contents were considered (**Table 3**). The ceramic radius increased from 7 to 18 mm in steps of 0.1 mm. Therefore, 5940 (54 × 110) treatments were set. Based on the computed electric field intensity and the given dielectric permittivity and electrical conductivity, $\varepsilon_{eff\text{-}C}$ and $\sigma_{eff\text{-}C}$ were determined using **Equation (21)** and **(22)**, respectively.

Table 3. *Ceramic-soil electrical conductivity combinations based on low, medium and high water contents. Note that the symbol ε_C represents apparent dielectric permittivity of ceramic, σ_C represents apparent electrical conductivity of ceramic, ε_S represents apparent dielectric permittivity of soil, σ_S represents apparent electrical conductivity of soil.*

Water content treatment	ε_C	σ_C (dS m^{-1})			ε_S		σ_S (dS m^{-1})		
low water content	3	0.01	0.02	0.03	2	5	0.01	0.02	0.03
medium water content	2	0.04	0.12	0.20	10	15	0.04	0.12	0.20
high water content	9	0.10	0.30	0.50	20	25	0.10	0.30	0.50

2.3.3. Verification for TDR sensitivity simulation

The validity of TDR sensitivity simulation was verified based on the experimental setup and measured data of Nissen et al. (2003). The effect of fluid level height on the ε_{eff} measurements were simulated and analyzed with a horizontally placed TDR. The study region was expanded to a square with a side length of 300 mm, and the medium boundary was adjusted to a horizontal line to represent the liquid-air interface. The bottom material was set as ethanol or water, corresponding to the dielectric permittivity of 25 and 80 respectively. The top boundary material was set as air, corresponding to the dielectric permittivity of 1. The rod radius and spacing were adjusted to 2.3 mm and 35 mm respectively. The simulation results were compared with the measurements.

2.4 Statistical analysis

The estimated physical properties based on COMSOL simulation (x_{eff}) were normalized:

$$x_n = \frac{x_{eff}}{x} \tag{23}$$

where x_n and x represent the normalized physical properties and the known reference values as preset for the medium in the simulation, respectively. Likewise, the absolute value of relative error (RE_a) was calculated to evaluate the influence of different sensor sizes on the accuracy:

$$RE_a = \left| \frac{x_{eff} - x}{x} \times 100\% \right| \tag{24}$$

Root means square error (*RMSE*) was used to compare the simulated temperature rise data with the measured data in the literatures:

$$RMSE = \sqrt{\frac{\sum_{i=1}^{n} \left(x_s - x_m \right)^2}{n}} \tag{25}$$

where x_s and x_m represent the simulated data based on COMSOL and measured data in the literatures, respectively, and n is the number of data points. To match the simulated data, the measure data were modified by using an interpolation function in Matlab.

3 Results and discussion

3.1 Simulation verification

3.1.1. Verification for heat pulse simulation

The temperature rise curves of DHPP heated water, dry sand and saturated sand were simulated and compared with the measurements of Kluitenberg et al. (2010). As shown in **Figure 3**, the simulated temperature rise curves were in good agreement with the measurements. However, the interference of many uncontrollable factors in the measurement leaded to error, including the thermal resistance of the contact between the rods and the dry sand for the dry sand cases. In the case of outward deflected rods for measuring saturated sand, the *RMSE* was 7.29×10^{-3} °C, which was the lowest, while in the case of outward deflected rods for measuring dry sand, the *RMSE* was 1.60×10^{-1} °C, which was the greatest. Even though, the *RMSE* were

within an acceptable range, which indicated that our COMSOL models were accurate and can be applied to the sensor optimization.

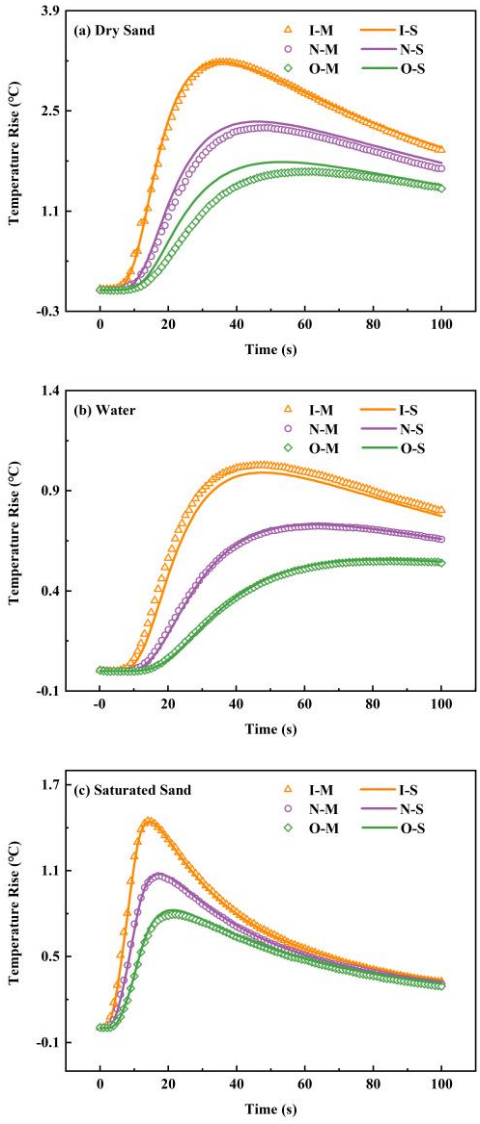

Figure 3. Measured (M) and simulated (S) temperature rise curves of dry sand, water, and saturated sand. All results were for the same DPHP sensor, with rods subjected to inward deflection (I), no deflection (N), and outward deflection (O). Measurements were retrieved from Mori et al. (2003) and Kluitenberg et al. (2010).

3.1.2. Verification of TDR sensitivity simulation

By comparing the dielectric permittivity measured by Nissen et al. (2003) at different liquid levels with our COMSOL simulation results, the feasibility of using COMSOL simulation to study TDR sensitivity was examined. The results of measurement and simulation are shown in **Figure 4**. The simulations deviated from

the measurements when the air-liquid boundary was at close proximity to the rod midpoint, although their trends were similar. The *RMSE* values were as low as 2.43 × 10^{-3} and 3.99 × 10^{-3} for water and ethanol, respectively. Therefore, our simulation can accurately and reliably predict TDR sensitivity and evaluate sensor accuracy.

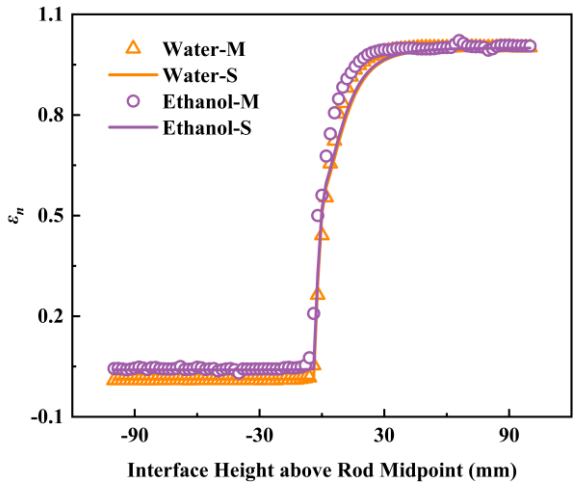

Figure 4. Measured (M) and simulated (S) normalized dielectric permittivity (ε_n) of water and ethanol for the air-liquid interface at difference distances related to the rod midpoint (0 indicates the air-liquid interface is located at the rod midpoint, positive and negative values indicate interface is above and below the rod midpoint, respectively). Data were retrieved from Nissen et al. (2003).

3.2 Simulation for thermal property estimations

3.2.1 Ceramic radius optimization for simulating thermal conductivity

The widely used ILS model is based on the assumption that the heat pulse sensors are embedded in an infinite and homogenous medium (Campbell et al. 1991; Philip and Kluitenberg 1999). The medium heterogeneity affects the heat transfer process, and therefore changes the temperature field, heat flux and temperature rise curve (Ren et al. 2005). The simulation results of temperature field and heat flux corresponding to different ceramic radii are shown in **Figure 5**. The porous ceramic matrix with a larger radius can retain more energy released by the heat pulse. Therefore, less of the heat propagates to the surrounding soil through radial heat transfer, which leads to lower estimation error. **Figure 6** shows the simulated ceramic temperature rise curves (i.e., temperature as a function of time) based on different

484 combinations of thermal properties of ceramic and soil. The ceramic temperature rises
485 shown in **Figure 6d** and **6g** were higher due to the higher C caused by the higher
486 ceramic water content, while in other cases the result was opposite due to the lower
487 ceramic water content. When the ceramic radius was 9 mm, the temperature rise
488 curves deviated noticeably. With the increase in ceramic radius, the deviation of the
489 temperature rise curves decreased until they tended to be constant. In addition, the
490 deviation degree of the temperature rise curves was affected by the difference in
491 thermal properties between the two mediums. As shown in **Figure 6a** and **6h**, the
492 temperature rise curves deviated slightly due to the similarity of the thermal properties
493 of soil and ceramic. On the contrary, the considerable difference in thermal properties
494 between the soil and ceramic increased the difficulty of obtaining accurate
495 temperature rise curves, such as **Figure 6c** and **6g**. For these cases, the ceramic radius
496 must be increased to improve the estimation accuracy.

497 **Figure 7** shows the normalized ceramic thermal conductivity ($\lambda_{n\text{-}C}$)
498 corresponding to 36 combinations of thermal properties. The $\lambda_{n\text{-}C}$ is inaccurate
499 because it is based on both the ceramic and the soil when the ceramic cross section is
500 smaller than the sampling area of the heat pulse. The positive or negative relative
501 error dependeds on the difference in thermal properties between the ceramic and the
502 soil, which is in agreement with **Figure 6**. Estimation accuracy improved with
503 increasing ceramic radius. The $\lambda_{n\text{-}C}$ was between 0.99 and 1.01 when the ceramic
504 radius ≥ 18 mm (**Figure 7**), which indicates that the RE_a caused by radial heat transfer
505 can be controlled within 1% when the ceramic radius is 18 mm. The theoretical
506 analysis of Campbell et al. (1991) showed that at the time corresponding to the
507 maximum temperature rise, the outer boundary with a temperature rise of 1% of the
508 maximum temperature rise was a circle with a radius of 2.37 r. The results of Ren et
509 al. (2005) indicated that the sampling area of the heat pulse was a circle with a radius
510 of 14 mm, i.e., 2.3 r. Thus, the optimal ceramic radius is larger than the theoretical
511 analysis and experimental results. This may be attributed to that considerable

difference in thermal properties between the soil and the ceramic are considered in our study. It should be noted that, in practice, the water contents of the ceramic and the soil are similar due to water equilibration, i.e., there are few cases where the thermal properties of the two mediums are noticeably different. Therefore, the ceramic radius of 18 mm can ensure high accuracy of the sensor (RE_a < 1%).

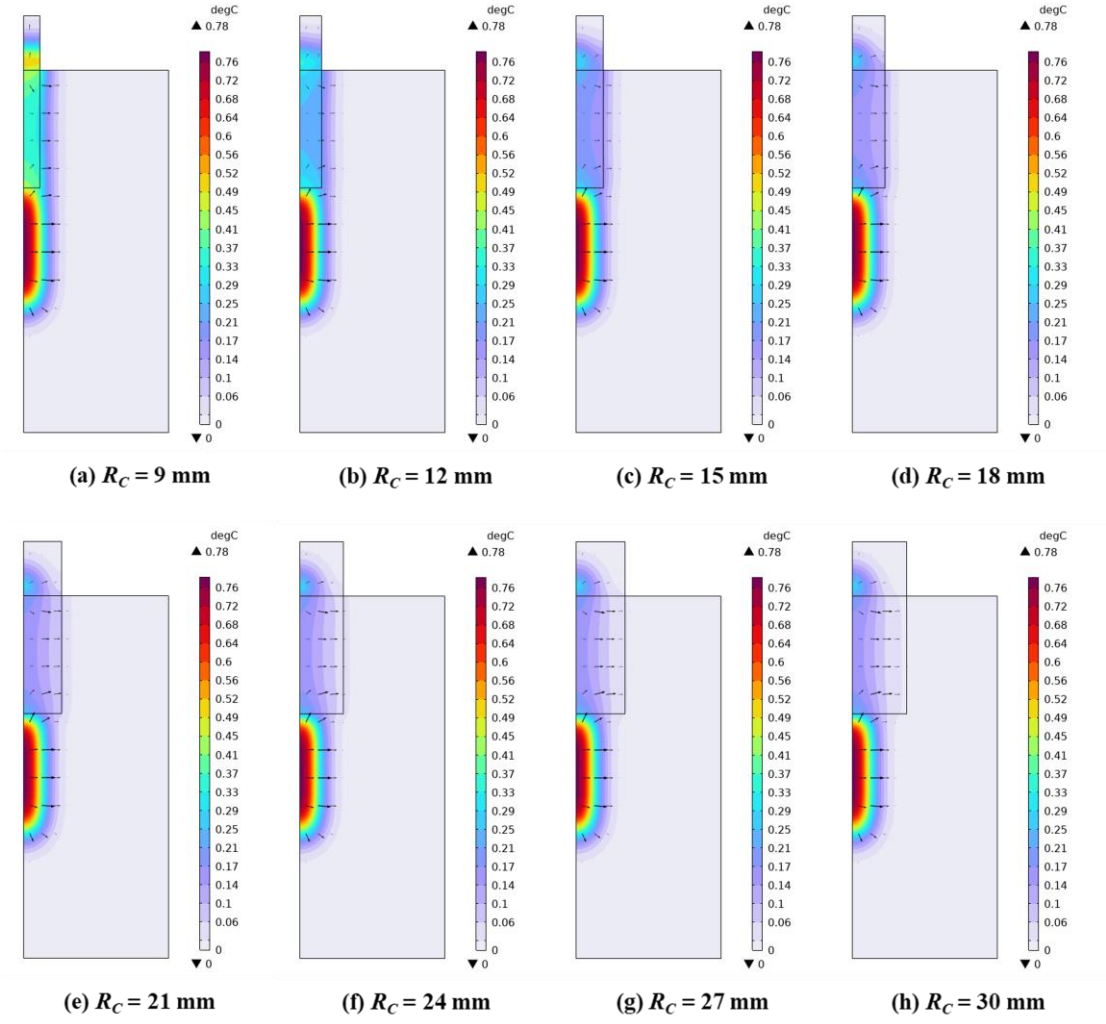

Figure 5. COMSOL simulated temperature distribution and heat flux at ceramic radius, R_C = 9, 12, 15, 18, 21, 24, 27 and 30 mm at 180 s after the 8-s heat input when ceramic thermal conductivity, λ_C = 0.35 W m^{-1} °C^{-1} and soil thermal conductivity, λ_s = 2.65 W m^{-1} °C^{-1}. Arrow direction represents direction of heat transfer, arrow size is proportional to magnitude of heat flux.

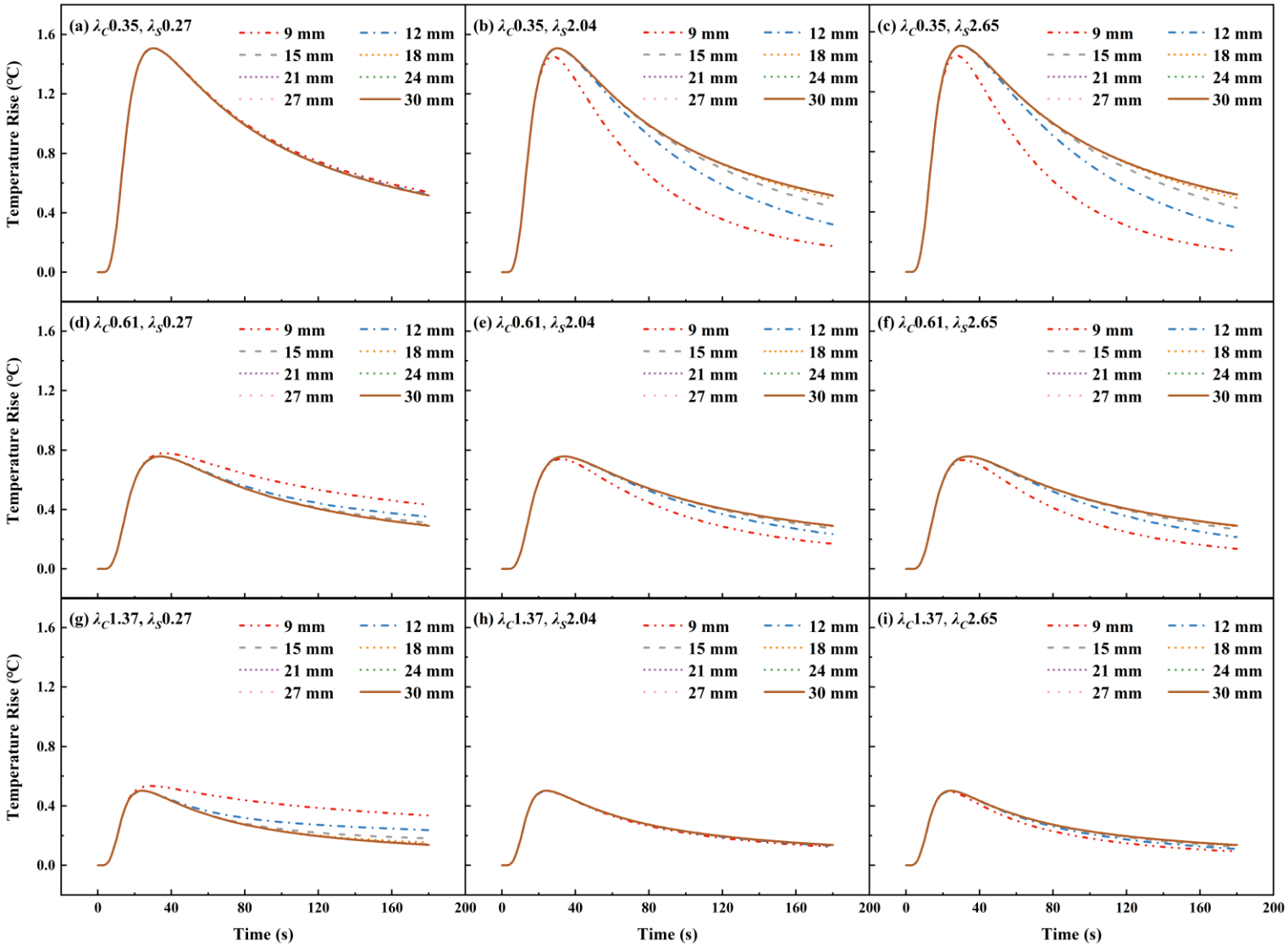

Figure 6. COMSOL simulated ceramic temperature rise as a function of time for different combinations of thermal conductivity of ceramic and soil. Ceramic thermal conductivity, λ_C that is set to be 0.35, 0.61 and 1.37 W m^{-1} $°C^{-1}$ and soil thermal conductivity, λ_S that is set to be 0.27, 2.04, and 2.65 W m^{-1} $°C^{-1}$; ceramic radius ranged from 9 to 30 mm. The data following λ_C or λ_S is the value of thermal conductivity (W m^{-1} $°C^{-1}$).

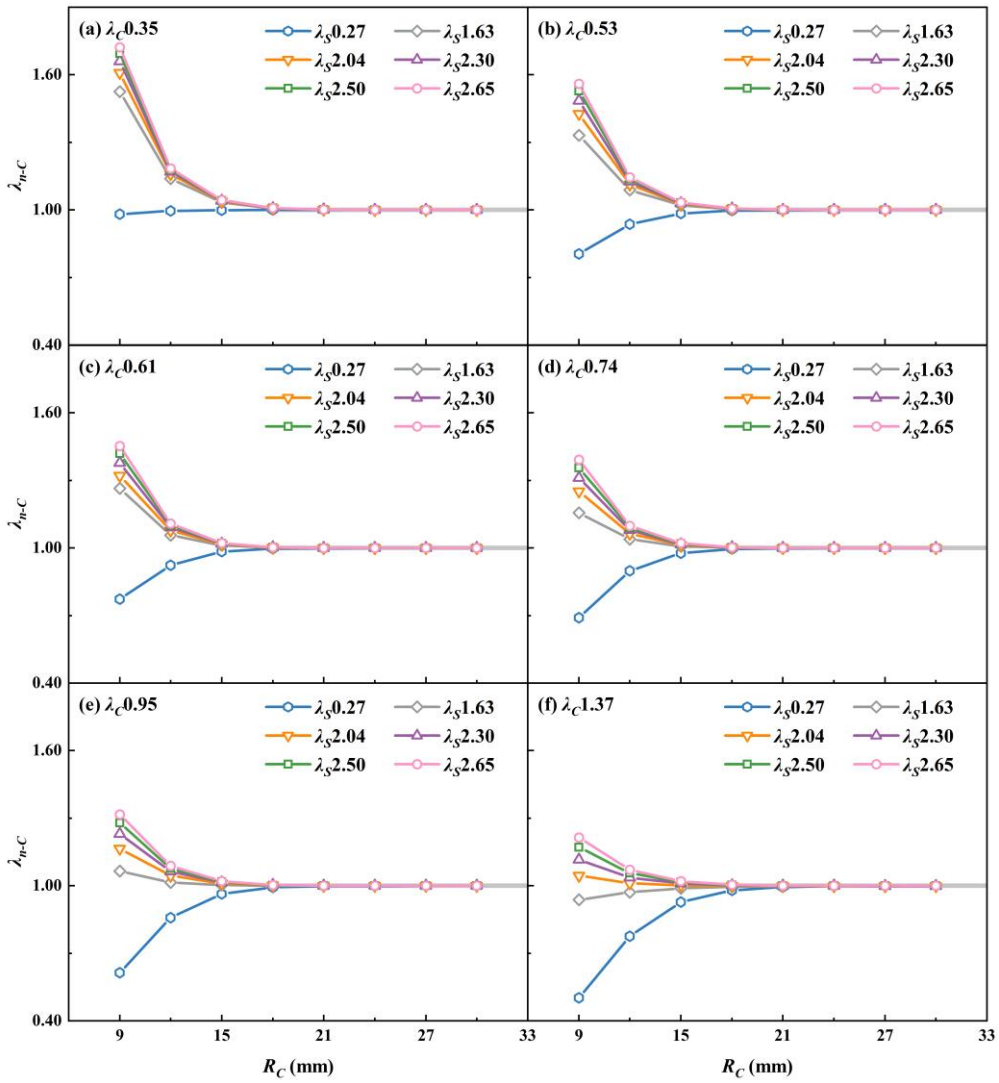

526

527 **Figure 7.** Normalized ceramic thermal conductivity ($\lambda_{n\text{-}C}$) as related to different ceramic radius
528 (R_C, with the settings of 9, 12, 15, 18, 21, 24, 27 and 30 mm) for different combinations of thermal
529 conductivity of ceramic (λ_C, ranging from 0.35 to 1.37 W m^{-1} °C^{-1}) and soil (λ_S, ranging from 0.27
530 to 2.65 W m^{-1} °C^{-1}), the unoptimized ceramic length and extended rod length is set to be 65 mm.
531 The data following λ_C or λ_S is the value of thermal conductivity (W m^{-1} °C^{-1}), and the regions with
532 the absolute value of relative error (RE_a) < 1% are marked with gray rectangle.

533 **3.2.2 Ceramic length optimization for simulating thermal conductivity**

534 **Figure 8** shows the results of the $\lambda_{n\text{-}C}$ corresponding to the 36 thermal property
535 combinations, with all results based on the ceramic radius of 18 mm. The error caused
536 by axial heat transfer decreased and the accuracy of thermal conductivity estimation
537 improved with increasing ceramic length. Some extreme cases were excluded, such as
538 soil thermal conductivity (λ_S) higher than 2.04 W m^{-1} in **Figure 8a** and λ_S of 0.27 W

m^{-1} in **Figure 8f**, because they represent the assumption that one medium is dry and the other medium is at a higher water content. Based on this, we found that the $\lambda_{n\text{-}C}$ was between 0.98 and 1.02 when the ceramic length ≥ 40 mm (as shown in the area marked by the gray rectangle in **Figure 8**), i.e., the RE_a caused by axial heat transfer can be controlled within 2%. Axial heat conduction occurred not only between the ceramic and the soil, but also between the handle and the soil. Meng et al. (2023) indicated that accurate measurement of thermal properties became more challenging as thermal properties of handle material increase relative to those of the measured medium. Therefore, the overestimation or underestimation of the λ_C did not completely correspond to the higher or lower λ_S, and the effect from the handle needs to be additionally considered. For example, in the case of **Figure 8f** where λ_S was higher than that of the ceramic, the λ_C may be underestimated, because of the large difference in thermal conductivity between the ceramic and the handle (the handle thermal conductivity was only 0.36 W m^{-1}). For the case in **Figure 8a** where the λ_S was 0.27 W m^{-1}, the temperature rise of the handle was less than that of the ceramic due to the high heat capacity of the handle and the short (10 mm) heat source in the handle. Due to the temperature gradient, more heat in the ceramic was transferred to the handle, which led to an overestimation of the λ_C.

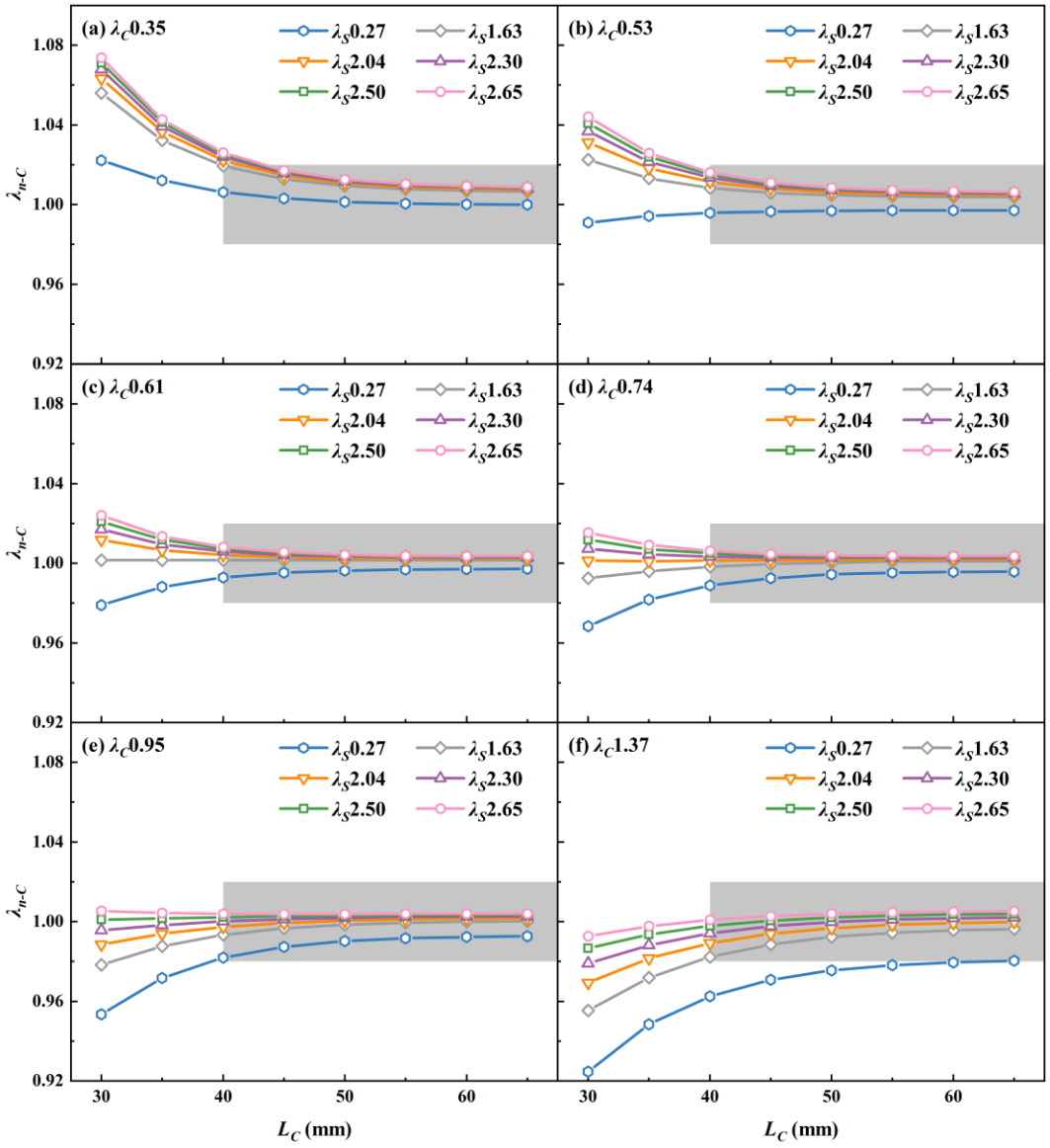

Figure 8. Normalized ceramic thermal conductivity ($\lambda_{n\text{-}C}$) as related to different ceramic lengths (L_C, with the settings of 30, 35, 40, 45, 50, 55, 60 and 65 mm) for different combinations of thermal conductivity of ceramic (λ_C, ranging from 0.35 to 1.37 W m^{-1} °C^{-1}) and soil (λ_S, ranging from 0.27 to 2.65 W m^{-1} °C^{-1}), the optimized ceramic radius and unoptimized extended rod length were set to 18 mm and 65 mm, respectively. The data following λ_C or λ_S is the value of thermal conductivity (W m^{-1} °C^{-1}), and the regions with the absolute value of relative error (RE_a) < 2% are marked with gray rectangle.

3.2.3 Optimization of the extended rod length for simulating thermal conductivity

The extended rod length was optimized based on the optimal ceramic radius and length. The relationship between normalized soil thermal conductivity ($\lambda_{n\text{-}S}$) and the extended rod length is shown in **Figure 9**. The accuracy of λ_S estimation improved with increasing extended rod length due to a decrease in the error caused by axial heat

transfer. However, considering the deflection problem caused by the long rods, the extended rod length of 50 mm was finally adopted. At the 50-mm extended rod length, the RE_a of λ_S estimation was less than 3% as shown in the regions marked by the gray rectangles in **Figure 9**, which was 3% lower than that of a traditional thermo-TDR with rod length of 40 mm (He et al. 2018). Therefore, our optimization considerably improved the sensor accuracy.

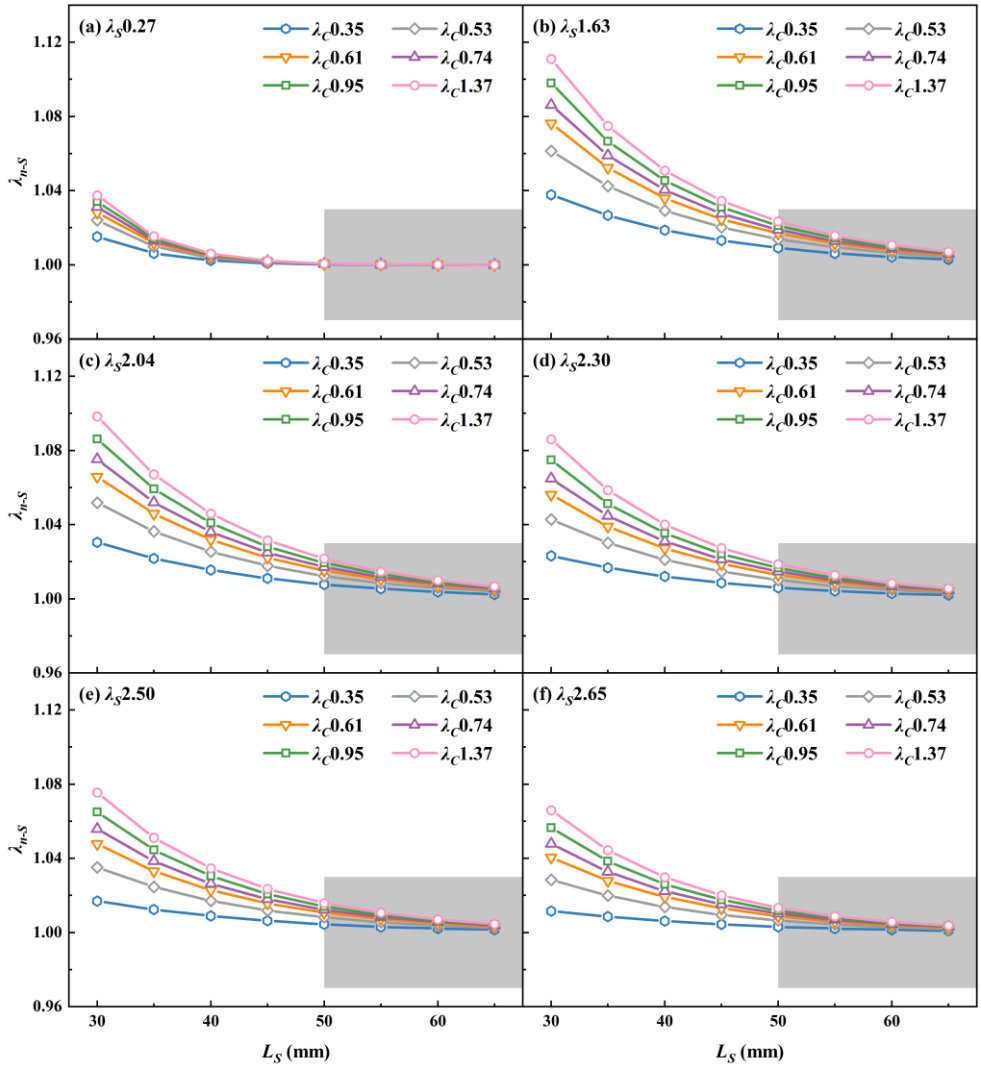

Figure 9. Normalized soil thermal conductivity ($\lambda_{n\text{-}S}$) as related to different extended rod length (L_S, with the settings of 30, 35, 40, 45, 50, 55, 60 and 65 mm) for different combinations of thermal conductivity of ceramic (λ_C, ranging from 0.35 to 1.37 W m^{-1} °C^{-1}) and soil (λ_S, ranging from 0.27 to 2.65 W m^{-1} °C^{-1}), the optimized ceramic radius and length were set to 18 mm and 40 mm, respectively. The data following λ_C or λ_S is the value of thermal conductivity (W m^{-1} °C^{-1}), and the regions with the absolute value of relative error (RE_a) < 3% are marked with gray rectangle.

584 For the cases of λ_S = 0.27 W m^{-1} °C^{-1}, the RE_as are lower than others as shown in
585 **Figure 9a**. The explanation may be that less heat was lost from the soil with low λ_S to
586 the surrounding medium during the temperature measurement, which resulted in a
587 smaller area of the soil affected by heat pulse. Unlike the ceramic optimization results,
588 the estimated errors were all positive, even if the λ_S was much lower than λ_C. This is
589 because the λ_S estimation is not only affected by the difference in thermal conductivity
590 between the two mediums, but also by the finite length of the heat source, and the
591 latter always contributes a positive error (Kluitenberg et al. 1993). Therefore, longer
592 extended rods will not only reduce the influence of medium heterogeneity on the
593 temperature measuring point, but also avoid deviation from the assumption of the heat
594 source of finite length. However, it is also noteworthy that long rods would be
595 affected by deflection when inserting into soils and significantly affect measurement
596 accuracy (Kluitenberg et al. 1993; Bristow et al. 1994; Kluitenberg et al. 1995).
597 The relative location of the temperature measuring point was defined as the ratio
598 of the distance from the temperature measuring point to the ceramic-soil boundary (*D,*
599 mm) to the extended rod length. The effect of the evaluated rod length and the relative
600 location of the temperature measuring point on the estimation of λs was evaluated,
601 and the results were shown in **Figure 10**. In the simulations, ceramic was represented
602 as soils (corresponding to the cases represented by dotted lines in **Figure 10**) to
603 exclude the effect of heterogeneity and evaluate the effect of the heat source of finite
604 length on the estimations. The results indicated that the positive error caused by heat
605 source of finite length increased with increasing value of D/L_S. The λ_n-s showed a
606 stable trend because the positive error caused by heterogeneity decreased with
607 increasing value of D/L_S (**Figure 10a)**. While the λ_n-s showed an increasing trend
608 because the negative error caused by heterogeneity decreased with increasing value of
609 D/L_S (**Figure 10b**). For The RE_a of the λs estimation was the lowest when D/L_S =0.50,
610 that is, the midpoint of the extended rode was the optimal temperature measuring
611 point (**Figure 10a**). While the RE_a of the λs estimation was the lowest when D/L_S =

0.49 (**Figure 10b**), that is, the location closer to the ceramic was the optimal temperature measuring point. The RE_a of the λs estimation can be controlled within 1.5% and 0.2% by extended rod length of 50 mm and 80 mm, respectively, that is, the RE_a can be effectively reduced by increasing extended rod length, which is consistent with the result in **Figure 9**.

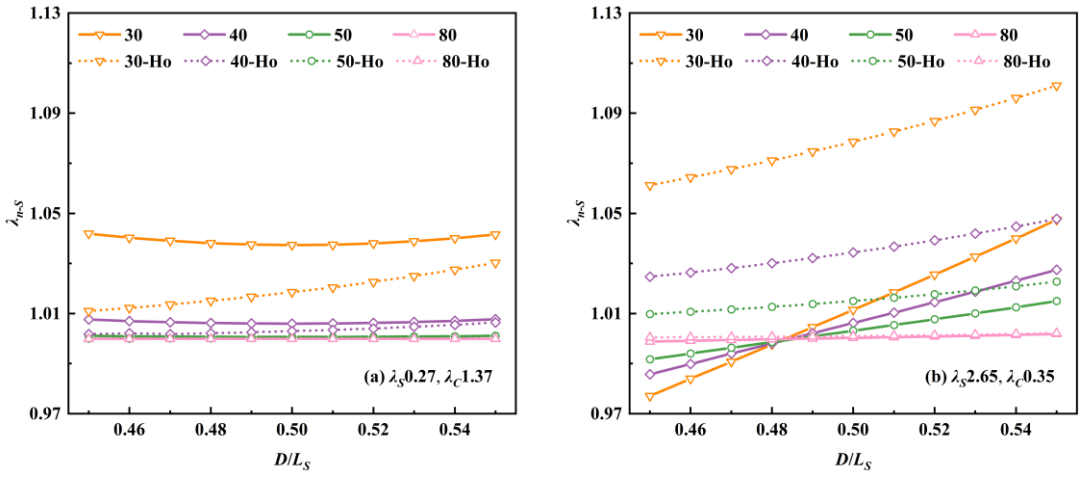

Figure 10. Normalized soil thermal conductivity ($\lambda_{n\text{-}S}$) related to the ratio of the distance from the temperature measuring point to the ceramic-soil boundary (D, mm) to the extended rod length (L_S, with the settings at 30, 40, 50 and 80 mm) for different combinations of thermal conductivity of ceramic (λ_C, with the settings of 0.35 and 1.37 W m^{-1} °C^{-1}) and soil (λ_S, with the settings of 0.27 and 2.65 W m^{-1} °C^{-1}), the optimized ceramic radius and length are set to 18 mm and 40 mm, respectively. The data following λ_C or λ_S is the value of thermal conductivity (W m^{-1} °C^{-1}), and the dotted lines represented cases in which the measured medium was homogeneous soil without ceramic (Ho).

3.2.4 Estimation accuracy of volumetric heat capacity

Figure 11 shows the normalized ceramic volumetric heat capacity ($C_{n\text{-}C}$) and normalized soil volumetric heat capacity ($C_{n\text{-}S}$) corresponding to the extreme thermal property combinations. Compared with thermal conductivity, volumetric heat capacity was more accurately estimated, even though the thermal properties of the ceramic and soil differ greatly. This is consistent with numerical analysis of Philip and Kluitenberg (1999) and the experimental results of Zhang et al. (2014), which indicated that the sensitivity of volumetric heat capacity data to heterogeneity is less than that of thermal conductivity data to heterogeneity when near-surface STP were measured by

heat pulse method.

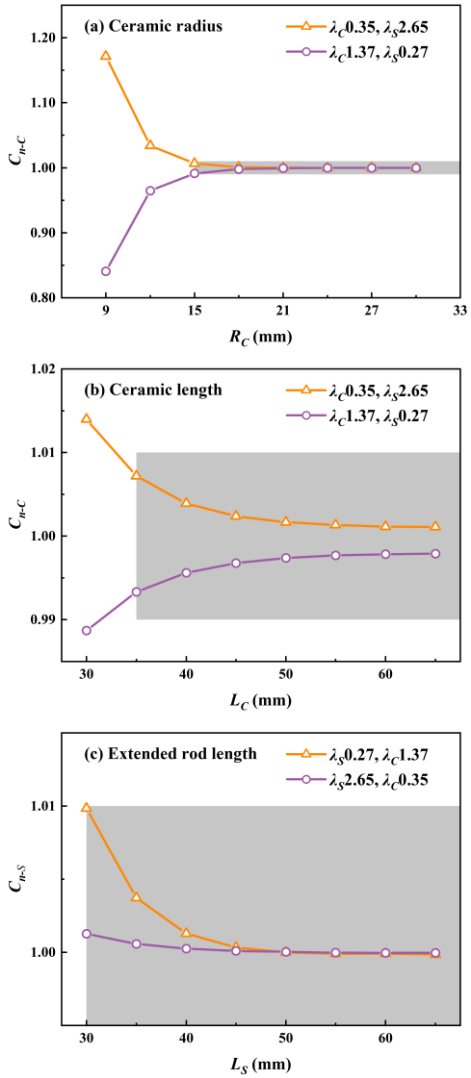

Figure 11. (a) normalized ceramic volumetric heat capacity ($C_{n\text{-}C}$) as related to ceramic radius (R_C), the unoptimized ceramic length (L_C) and extended rod length (L_S) are set to be 65 mm; (b) $C_{n\text{-}C}$ as related to L_C, the optimized R_C and unoptimized L_S are set to 18 mm and 65 mm, respectively; and (c) normalized soil volumetric heat capacity ($C_{n\text{-}S}$) as related to L_S, the optimized R_C and L_C are set to 18 mm and 40 mm, respectively, when different combinations of thermal conductivity of ceramic (λ_C, 0.35 and 1.37 W m^{-1} °C^{-1}) and soil (λ_S, 0.27 and 2.65 W m^{-1} °C^{-1}) for. The data following λ_C or λ_S is the value of thermal conductivity (W m^{-1} °C^{-1}), and the regions with the absolute value of relative error (RE_a) < 1% are marked with gray rectangle.

The RE_a of estimated ceramic volumetric heat capacity caused by radial and axial heat transfer can be controlled within 1 % when the $R_C \geq 15$ mm and $L_C \geq 35$ mm, respectively. The RE_a of estimation of soil volumetric heat capacity caused by axial heat transfer and finite length of the heat source can be controlled within 1%

when $L_S \geq 30$ mm. Similar to the soil thermal conductivity, the soil volumetric heat capacity was always overestimated, which was also due to the limited length of the heat source (Kluitenberg et al. 1993). Therefore, the optimized sensor sizes (ceramic radius of 18 mm, ceramic length of 40 mm and extended rod length of 50 mm) based on ceramic and soil thermal conductivity estimations can ensure a low RE_a (< 1%) of ceramic and soil volumetric heat capacity estimation.

3.3 Simulations for the estimations of ceramic dielectric permittivity and electrical conductivity

3.3.1 Ceramic radius optimization for dielectric permittivity estimations

Similar to thermal property estimation, the medium heterogeneity affects the electric field, and therefore leads to errors in estimating dielectric permittivity and electrical conductivity. The simulation results of electric field corresponding to different ceramic radii are shown in **Figure 12**. The porous ceramic matrix with a large radius can contain more energy released by the central rod. Therefore, less of the energy prorogates to the surrounding soil and leads to lower estimation error. **Figure 13** shows the results of ceramic radius optimization based on ε_C estimations. As ceramic radius increased, normalized ceramic dielectric permittivity ($\varepsilon_{n\text{-}C}$) gradually approached 1. The $\varepsilon_{n\text{-}C}$ was between 0.99 and 1.01 when the ceramic radius ≥ 13 mm, as shown in regions marked by the gray rectangles in **Figure 13**.The RE_a caused by the difference in dielectric permittivity between the ceramic and the soil can be controlled within 1% when the ceramic radius is 13 mm. The sampling radius of the TDR with a rod diameter of 1.3 mm and a spacing of 6 mm is 11 mm, the associated RE_a of ε_C was 2%, which is in good agreement with Ren et al. (2005).

A soil differing considerably in dielectric permittivity from the ceramic results in a higher ε_C estimations error. For example, the RE_as of ε_C estimation at ε_S of 2 (blue hexagons), 5 (gray diamonds), 20 (green squares), and 25 (pink circles) at R_C = 7 mm, were 11 %, 6 %, 2 %, and 3 %, respectively, which were higher than those of 1% at ε_S = 10 (orange triangles) and 15 (purple triangles) as indicated by **Figure 13d**. In

addition to the considerable dielectric permittivity difference between the two mediums, a high RE_a may also be caused by a soil with a low dielectric permittivity. The RE_a of ε_C estimation at ε_S = 2 (blue hexagons) was 7 % at R_C = 7 mm, which was higher than that of 3 % at ε_S =25 (pink circles), even though the dielectric permittivity of the two mediums were more similar in the former case as shown in **Figure 13b**. Similarly, the RE_a of ε_C estimation at ε_S = 10 (orange triangles) was 3 % at R_C = 7 mm, which was higher than that of 2% at ε_S = 25 (pink circles) as shown in **Figure 13a**. This is because the measurement sensitivity is biased toward the lower permittivity region, as the soil with lower dielectric permittivity shows a higher contribution to $\varepsilon_{eff\text{-}C}$. This bias arises because the potential gradient of the energy through the region with low dielectric permittivity is much higher than that through the region with high dielectric permittivity. This is also shown by the simulation results in **Figure 12a**, **12b**, and **12c**, where some soil regions have higher electric field intensity than the ceramic on the edge due to its their lower dielectric permittivity although the soil is further away from the central rod than the ceramic. According to **Eq. (13)**, a high potential gradient means that the energy and the sensitivity is concentrated within the region with low dielectric permittivity (Nissen et al. 2003). Numerical analysis indicates that the interference medium with low dielectric permittivity has a greater impact on the measured dielectric permittivity than the interference medium with high dielectric permittivity (Knight et al. 1997). Therefore, the soil with low dielectric permittivity and a considerable difference from ε_C result in a high RE_a of ε_C estimation. For example, the RE_a of ε_C estimation (12%) was the highest of all cases for ε_S = 2 and R_C = 7 mm (**Figure 13f**).

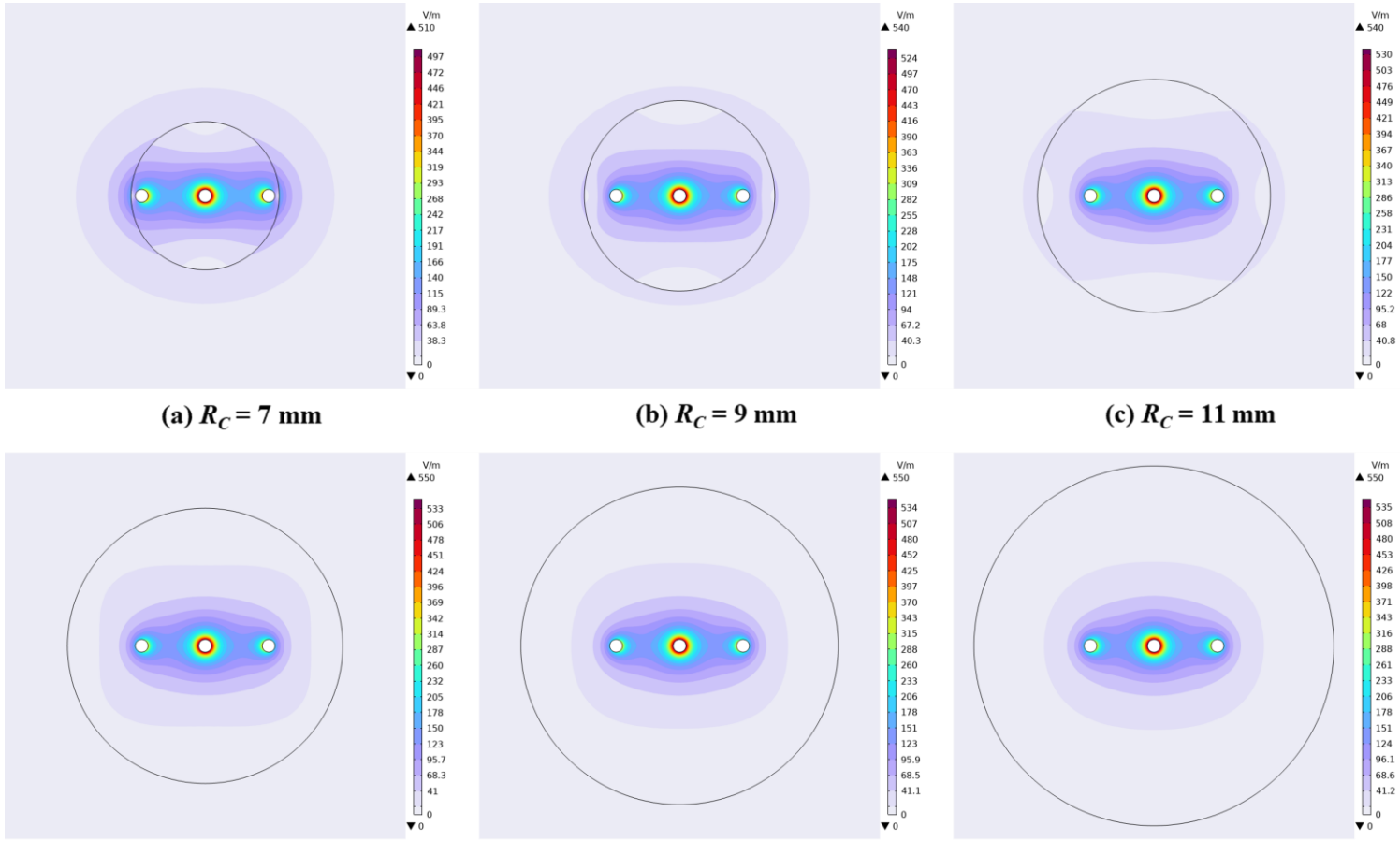

Figure 12. The simulated electric field intensity at ceramic radius, R_C = 7, 9, 11, 13, 15 and 17 mm for the case of ceramic dielectric permittivity of 19 and soil dielectric permittivity of 2. Circles represent the ceramic-soil boundary.

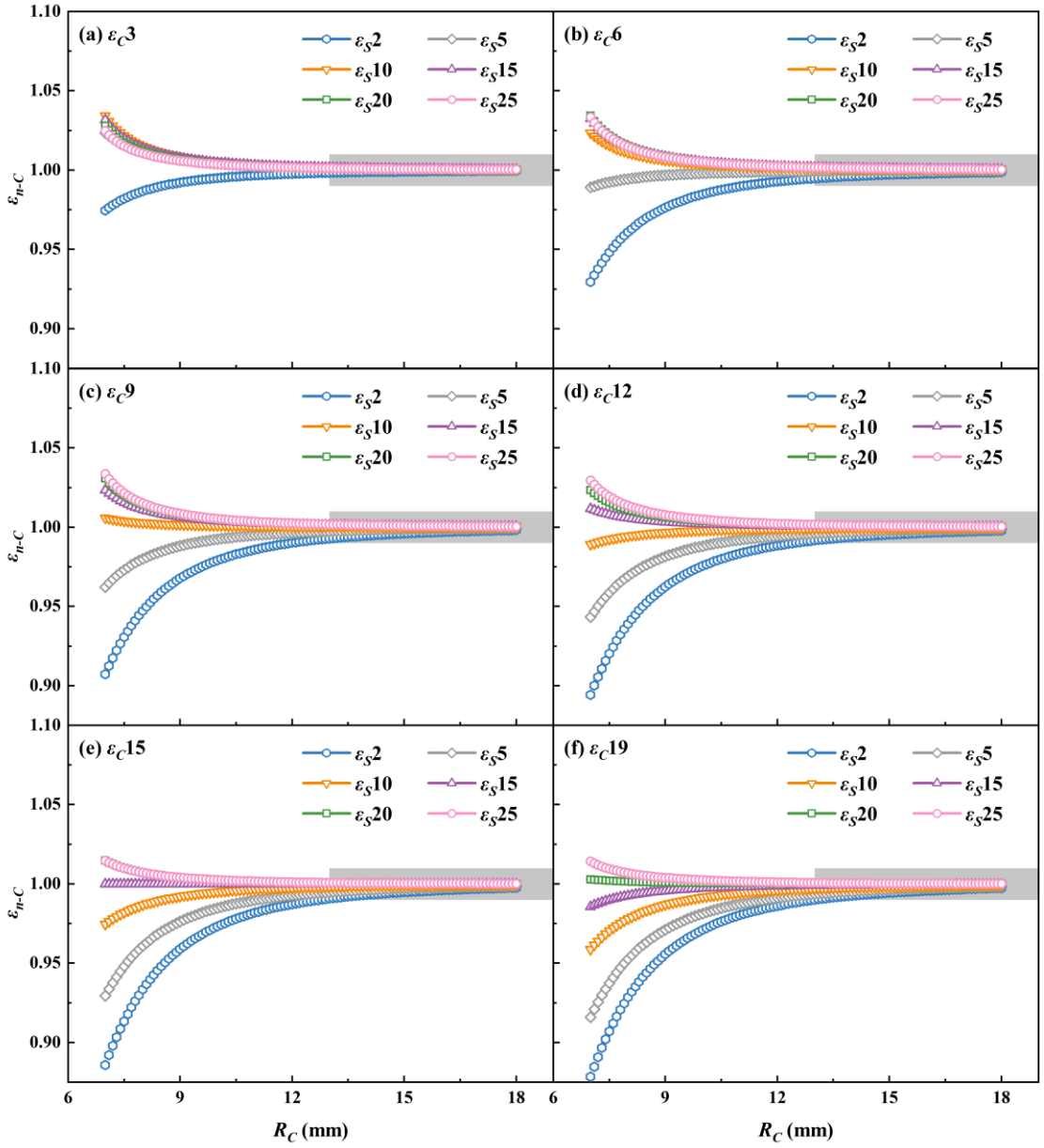

703

704 **Figure 13.** Normalized ceramic dielectric permittivity ($\varepsilon_{n\text{-}C}$) as related to ceramic radius (R_C,
705 ranging from 7 to 18 mm) for different combinations of ceramic dielectric permittivity (ε_C,
706 ranging from 3 to 19) and soil dielectric permittivity (ε_S, ranging from 2 to 25). The data following
707 ε_C or ε_S is the value of dielectric permittivity, and the regions with the absolute value of relative
708 error (RE_a) < 1% are marked with gray rectangle.

709 **3.3.2 Ceramic radius optimization for electrical conductivity estimations**

710 **Figure 14** shows the relationship between normalized ceramic electrical
711 conductivity ($\sigma_{n\text{-}C}$) and ceramic radius. When the ceramic radius was small, the RE_a of
712 σ_C estimation was high; conversely, the error decreased with increasing ceramic

radius. The RE_a was controlled within 1% for a radius up to 14.8 mm, as shown in the and regions marked by the gray rectangles (**Figure 14**).

According to **Eq.** (22), the error source of σ_C estimation was similar to that for ε_C, including the difference in values between ε_C and ε_S and the contribution of soil to $\varepsilon_{eff\text{-}C}$. Since the contribution level of the soil to $\sigma_{eff\text{-}C}$ was calculated based on the dielectric permittivity of the two mediums, $\sigma_{eff\text{-}C}$ was affected by the dielectric permittivity of the two mediums as well as their electrical conductivity. In **Figure 14g**, due to the greater difference in electrical conductivity between the soil and the ceramic, the RE_a of σ_C estimation at R_C = 7 mm was 22% for ε_S = 20 and σ_S = 0.50 (orange triangles), which was higher than 11% for ε_S =20 and σ_S = 0.30 (gray diamonds). Due to the lower ε_S, in the case of ε_S = 20 and σ_S = 0.50 (orange triangles) in **Figure 14**, at R_C = 7 mm, the RE_a of σ_C estimation of 22% is greater than that of 18% corresponding to the case of ε_S = 25 and σ_S = 0.50 (pink circles). Nissen et al. (2001) and Ferré et al. (2003) indicated that the sensitivity of TDR to electrical conductivity measurement was independent of the conductivity distribution of the medium. This conclusion differs from ours is that the interfering medium was not soil in their study, but air with electrical conductivity of 0. In this case, the part of "$\sigma_S \times MSS$" in **Eq. (22)** is equal to 0, and $\varepsilon_{eff\text{-}C}$ is only affected by the dielectric permittivity distribution, independent of the electrical conductivity distribution. The $\sigma_{n\text{-}C}$ is therefore equal to the contribution level of the measured medium to $\varepsilon_{eff\text{-}C}$, i.e., MSC in **Eq. (18)**.

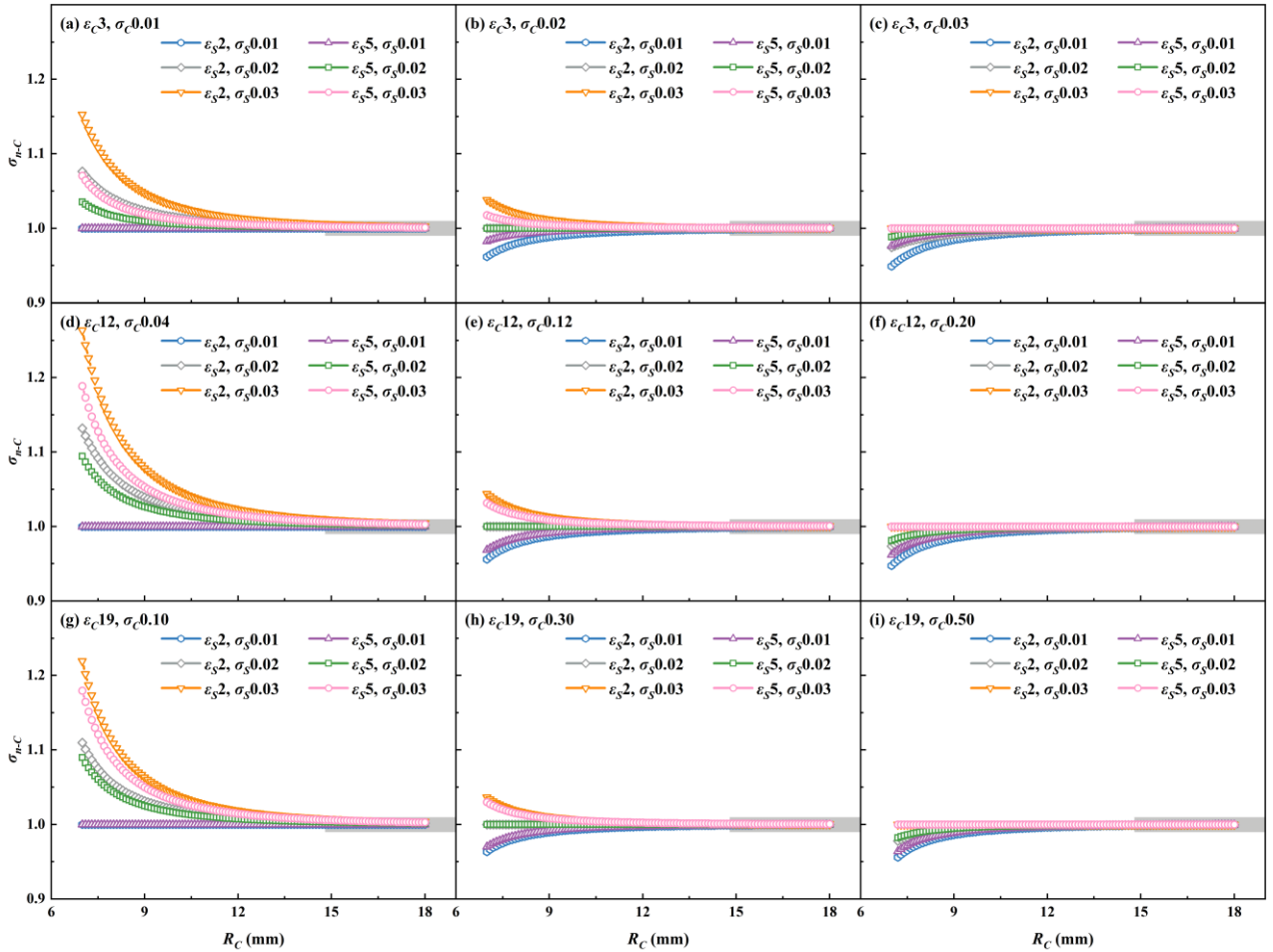

734

735 **Figure 14.** Normalized ceramic electrical conductivity ($\sigma_{n\text{-}C}$) as related to ceramic radius (R_C, ranging from 7 to 18 mm) for different combinations of ceramic
736 dielectric permittivity (ε_C= 3, 12, and 19), soil dielectric permittivity (ε_S=2 and 5), ceramic electrical conductivity (σ_C= 0.1, 0.3 and 0.5 dS m^{-1}) and soil electrical
737 conductivity (σ_S= 0.01, 0.02 and 0.03 dS m^{-1}). The data following ε_C or ε_S is the value of dielectric permittivity, the data following σ_C or σ_S is the value of electrical
738 conductivity (dS m^{-1}), and the regions with the absolute value of relative error (RE_a) < 1% are marked with gray rectangle.

4 Conclusion

A multifunctional sensor was developed by coupling heat pulse, TDR and matric potential sensors to simultaneously measure soil water content, matric potential and thermal properties of the same soil sample. The soil water content and thermal properties are measured directly by the rods extended out of the ceramics, while the soil matric potential can be predicted indirectly based on the thermal conductivity, volumetric heat capacity, water content or electrical conductivity of the porous ceramic matrix. Compared with the measured data in the literatures, our COMSOL models were verified to be able to accurately and reliably evaluate the sensor error and optimize the sensor. The simulation results indicated that a high estimation accuracy can be attained by increasing the size of the porous ceramic matrix, even in the presence of considerable differences in physical properties between the soil and the ceramic matrix. Our optimization results indicate that the optimal design for the porous ceramic matrix was a cylinder with a radius of 18 mm and a height of 40 mm and the heat pulse sensor extended a rod length of 50 mm out of the ceramics. This design ensures that the estimation errors for dielectric permittivity, electrical conductivity, thermal conductivity and volumetric heat capacity of the porous ceramic matrix are within acceptable ranges. The optimized multifunctional sensor was high in accuracy, low in cost and non-destructive. More importantly, the sensor can simultaneously measure soil hydrothermal properties accounting for temporal and spatial variability of soil, which is of great significance for the better understating and modeling of coupled water, heat and solute transport.

List of symbols

C	volumetric heat capacity	M J m^{-3} °C^{-1}
$C_{n\text{-}C}$	normalized ceramic volumetric heat capacity	unitless
$C_{n\text{-}S}$	normalized soil volumetric heat capacity	unitless
D	distance from the temperature measuring point to	mm

	the ceramic-soil boundary	
$E(x, y)$	electric field intensity	V/m
L	rod length	mm
L_C	ceramic length	mm
L_{max}	the maximum rod length	m
L_{min}	the maximum rod length	m
L_S	length of the extended rod buried in soil	mm
p	porosity	unitless
Q	rate per unit volume of heat generation for the numerical model	$W\ m^{-3}$
S_H	cross-sectional area of the heater	m^2
T	temperature	℃
V_T	excitation voltage	V
V_R	reflected voltage	V
c	specific heat	$J\ kg^{-1}\ ℃^{-1}$
c_w	specific heat of water	$4180\ J\ kg^{-1}\ ℃^{-1}$
d	rod diameter	mm
f_{sa}	sand fraction for soil solids	%
n	number of data points	unitless
q'	heat strength	$W\ m^{-1}$
qc	quartz content of the total solids content	unitless
r	rod spacing	mm
t	time	s
t_0	duration	s
t_e	travel time of electromagnetic wave	s
v_0	velocity of light in a vacuum	$3 \times 10^8\ m\ s^{-1}$
$w(x, y)$	spatial weighting factor	m^{-2}
$w_C(x, y)$	weighting factors that are distributed in the ceramic region	m^{-2}
$w_S(x, y)$	weighting factors that are distributed in the soil region	m^{-2}
x	reference physical properties as preset for the medium in the simulation,	/

x_{eff}	estimated physical properties based on COMSOL simulation	/
x_m	measured data in the literatures	/
x_n	normalized physical properties	/
x_s	simulated data based on COMSOL	/
β	empirical parameter	unitless
ε	dielectric permittivity	unitless
ε_C	apparent dielectric permittivity of ceramic	unitless
ε_S	apparent dielectric permittivity of soil	unitless
ε_{eff}	effective dielectric permittivity	unitless
ε_n	normalized dielectric permittivity	unitless
$\varepsilon_{n\text{-}C}$	normalized ceramic dielectric permittivity	unitless
θ	water content	$cm^3\ cm^{-3}$
κ	thermal diffusivity	$m^2\ s^{-1}$
λ	thermal conductivity	$W\ m^{-1}\ ℃^{-1}$
λ_C	ceramic thermal conductivity	$W{\cdot}m^{-1}{\cdot}℃^{-1}$
λ_{dry}	dry thermal conductivity	$W{\cdot}m^{-1}{\cdot}℃^{-1}$
$\lambda_{n\text{-}C}$	normalized ceramic thermal conductivity	unitless
$\lambda_{n\text{-}S}$	normalized soil thermal conductivity	unitless
λ_o	thermal conductivity of other minerals	$W{\cdot}m^{-1}{\cdot}℃^{-1}$
λ_S	soil thermal conductivity	$W{\cdot}m^{-1}{\cdot}℃^{-1}$
λ_q	thermal conductivity of quartz	$7.7\ W\ m^{-1}\ ℃^{-1}$
λ_{sat}	saturated thermal conductivity	$W{\cdot}m^{-1}{\cdot}℃^{-1}$
λ_{solids}	thermal conductivity of solids	$W{\cdot}m^{-1}{\cdot}℃^{-1}$
λ_w	thermal conductivity of water	$0.594\ W\ m^{-1}\ ℃^{-1}$ at 20 ℃
ρ	wet bulk density	$kg\ m^{-3}$
ρ_b	bulk density	$kg\ m^{-3}$
$\rho_{solids}c_{solids}$	volumetric heat capacity of solids	$M\ J\ m^{-3}\ ℃^{-1}$
ρ_w	density of water	$1000\ kg\ m^{-3}$
σ	electrical conductivity	$dS\ m^{-1}$
σ_C	apparent electrical conductivity of ceramic	$dS\ m^{-1}$
σ_S	apparent electrical conductivity of soil	$dS\ m^{-1}$

σ_{eff}	effective electrical conductivity	unitless
$\sigma_{n\text{-}C}$	normalized ceramic electrical conductivity	unitless
ψ_m	matric potential	kpa
$\nabla\Phi(x, y)$	potential gradients in homogeneous fields	V/m
$\nabla\Phi_0(x, y)$	potential gradients in heterogeneous fields	V/m

Author contributions

HH conceptualized the study; JH and JC wrote the original paper; HH, YC, CZ ,LJ, ZC and FZ reviewed and revised the manuscript. All authors contributed to the discussions and provided feedback on the final version.

Acknowledgements

Funding for this research was provided in part by the National Natural Science Foundation of China [Grant No.42177291], Innovation Capability Support Program of Shaanxi Province (2023-JC-JQ-25 and 2021KJXX-11), and high-End Foreign Experts Project from the Ministry of Science and Technology, China (G2023172014L). Thanks go to Prof. Lin Zhang, Mr. Qi Liu, Ms. Xuefei He and Ms. Juan Yu for their guidance on the preparation of porous ceramic.

Data availability statement

Data generated in this study is available at https://zenodo.org/records/10529525.

Conflicts of interest

The authors declare no conflict of interest.

References

Bristow, K. L. (2002), 5.3 Thermal Conductivity, in *Methods of Soil Analysis: Part 4. Physical Methods, Soil Science Society of America. Book Series*. *5*, edited by J. H. Dane, & G. C. Topp, pp. 1209–1226, Soil Science Society of America, Madison, WI. https://doi.org/10.2136/sssabookser5.4.c5

Bristow, K. L., Kluitenberg, G. J., & Horton, R. (1994). Measurement of soil thermal properties with a dual-probe heat-pulse technique. *Soil Science Society of America Journal*, *58*(5), 1288–1294. https://doi.org/10.2136/sssaj1994.03615995005800050002x

Brocca, L., Moramarco, T., Melone, F., & Wagner, W. (2013). A new method for rainfall estimation through soil moisture observations. *Geophysical Research Letters*, *40*(5), 853–858. https://doi.org/10.1002/grl.50173

Bruvik, E., Hjertaker, B., Folgerø, K., & Meyer, S. (2012). Monitoring oil-water mixture separation by time domain reflectometry. *Measurement Science and Technology*, *23*(12), 125303. https://doi.org/10.1088/0957-0233/23/12/125303

Bwambale, E., Abagale, F. K., & Anornu, G. K. (2022). Smart irrigation monitoring and control strategies for improving water use efficiency in precision agriculture: A review. *Agricultural Water Management*, *260*, 107324. https://doi.org/10.1016/j.agwat.2021.107324

Campbell, G., Calissendorff, C., & Williams, J. (1991). Probe for measuring soil specific heat using a heat-pulse method. *Soil Science Society of America Journal*, *55*(1), 291–293. https://doi.org/10.1016/j.agwat.2021.107324

Campbell, G. S., & Gee, G. W. (1986), Water potential: miscellaneous methods, in *Methods of Soil Analysis: Part 1 Physical and Mineralogical Methods*. *5*, edited by A. Klute, pp. 619–633, American Society of Agronomy, Madison, WI. https://doi.org/10.2136/sssabookser5.1.2ed.c25

Dalton, F., Herkelrath, W., Rawlins, D., & Rhoades, J. (1984). Time-domain reflectometry: Simultaneous measurement of soil water content and electrical conductivity with a single probe. *Science*, *224*(4652), 989–990. https://doi.org/10.1126/science.224.4652.989

Dalton, F., & Van Genuchten, M. T. (1986). The time-domain reflectometry method for measuring soil water content and salinity. *Geoderma*, *38*(1–4), 237–250. https://doi.org/10.1016/0016-7061(86)90018-2

Datta, S., & Taghvaeian, S. (2023). Soil water sensors for irrigation scheduling in the United States: A systematic review of literature. *Agricultural Water Management*, *278*, 108148. https://doi.org/10.1016/j.agwat.2023.108148

Ferré, T. P., Nissen, H. H., Knight, J. H., & Moldrup, P. (2003). Transverse sample area of two-and three-rod time domain reflectometry probes: Electrical conductivity. *Water Resources Research*, *39*(9), 1261. https://doi.org/10.1029/2002WR001572

Hamed, Y., Persson, M., & Berndtsson, R. (2003). Soil solution electrical conductivity

measurements using different dielectric techniques. *Soil Science Society of America Journal*, *67*(4), 1071–1078. https://doi.org/10.2136/sssaj2003.1071

He, H., Aogu, K., Li, M., Xu, J., Sheng, W., Jones, S. B., et al. (2021). A review of time domain reflectometry (TDR) applications in porous media. *Advances in Agronomy*, *168*, 83–155. https://doi.org/10.1016/bs.agron.2021.02.003

He, H., Dyck, M., Horton, R., Ren, T., Bristow, K. L., Lv, J., et al. (2018). Development and Application of the Heat Pulse Method for Soil Physical Measurements. *Reviews of Geophysics*, *56*(4), 567–620. https://doi.org/10.1029/2017RG000584

He, H., Dyck, M., Wang, J., & Lv, J. (2015). Evaluation of TDR for quantifying heat-pulse-method-induced ice melting in frozen soils. *Soil Science Society of America Journal*, *79*(5), 1275–1288. https://doi.org/10.2136/sssaj2014.12.0499

He, H., Li, M., Dyck, M., Si, B., Wang, J., & Lv, J. (2020). Modelling of soil solid thermal conductivity. *International Communications in Heat and Mass Transfer*, *116*, 104602. https://doi.org/10.1016/j.icheatmasstransfer.2020.104602

He, H., Zhao, Y., Dyck, M. F., Si, B., Jin, H., Lv, J., et al. (2017). A modified normalized model for predicting effective soil thermal conductivity. *Acta Geotechnica*, *12*, 1281–1300. https://doi.org/10.1007/s11440-017-0563-z

He, H., Zou, W., Jones, S. B., Robinson, D. A., Horton, R., Dyck, M., et al. (2023). Critical review of the models used to determine soil water content using TDR-measured apparent permittivity. *Advances in Agronomy*, *182*, 169–219. https://doi.org/10.1016/bs.agron.2023.06.004

Johansen, O. (1975). Thermal conductivity of soils (PhD thesis) (pp. 236). University of Trondheim.

Kamai, T., & Hopmans, J. W. (2007). Coupled heat and water flow in variably-saturated porous media. In Proceedings of the COMSOL Conference, Boston.

Kamai, T., Kluitenberg, G. J., & Hopmans, J. W. (2015). A dual-probe heat-pulse sensor with rigid probes for improved soil water content measurement. *Soil Science Society of America Journal*, *79*(4), 1059–1072. https://doi.org/10.2136/sssaj2015.01.0025

Kargas, G., & Soulis, K. X. (2019). Performance evaluation of a recently developed soil water content, dielectric permittivity, and bulk electrical conductivity electromagnetic sensor. *Agricultural Water Management*, *213*, 568–579. https://doi.org/10.1016/j.agwat.2018.11.002

Kluitenberg, G. (2002), 5.2 Heat capacity and specific heat, in *Methods of Soil Analysis: Part 4. Physical Methods, Soil Science Society of America. Book Series*. *5*, edited by J. H. Dane, & G. C. Topp, pp. 1201–1226, Soil Science Society of America, Madison, WI. https://doi.org/10.2136/sssabookser5.4.c49

Kluitenberg, G., Bristow, K. L., & Das, B. (1995). Error analysis of heat pulse method for measuring soil heat capacity, diffusivity, and conductivity. *Soil Science Society of America Journal*, *59*(3), 719–726. https://doi.org/10.2136/sssaj1995.03615995005900030013x

Kluitenberg, G. J., Ham, J. M., & Bristow, K. L. (1993). Error analysis of the heat pulse method

for measuring soil volumetric heat capacity. *Soil Science Society of America Journal*, *57*(6), 1444–1451. https://doi.org/10.2136/sssaj1993.03615995005700060008x

Kluitenberg, G. J., Kamai, T., Vrugt, J. A., & Hopmans, J. W. (2010). Effect of probe deflection on dual-probe heat-pulse thermal conductivity measurements. *Soil Science Society of America Journal*, *74*(5), 1537–1540. https://doi.org/10.2136/sssaj2010.0016N

Knight, J. (1992). Sensitivity of time domain reflectometry measurements to lateral variations in soil water content. *Water Resources Research*, *28*(9), 2345–2352. https://doi.org/10.1029/92wr00747

Knight, J., Ferré, P., Rudolph, D., & Kachanoski, R. (1997). A numerical analysis of the effects of coatings and gaps upon relative dielectric permittivity measurement with time domain reflectometry. *Water resources research*, *33*(6), 1455–1460. https://doi.org/10.1029/97wr00435

Kodešová, R., Vlasakova, M., Fer, M., Tepla, D., Jakšík, O., Neuberger, P., et al. (2013). Thermal properties of representative soils of the Czech Republic. *Soil and Water Research*, *8*(4), 141–150. https://doi.org/10.17221/33/2013-swr

Kojima, Y., Kawashima, T., Noborio, K., Kamiya, K., & Horton, R. (2021). A dual-probe heat pulse-based sensor that simultaneously determines soil thermal properties, soil water content and soil water matric potential. *Computers and Electronics in Agriculture*, *188*, 106331. https://doi.org/10.1016/j.compag.2021.106331

Kojima, Y., Matsuoka, M., Ariki, T., & Yoshioka, T. (2023). Time Domain Transmissiometry-Based Sensor for Simultaneously Measuring Soil Water Content, Electrical Conductivity, Temperature, and Matric Potential. *Sensors*, *23*(4), 2340. https://doi.org/10.3390/s23042340

Kojima, Y., Noborio, K., Mizoguchi, M., & Kawahara, Y. (2017). Matric potential sensor using dual probe heat pulse technique. *Agricultural Information Research*, *26*(4), 77–85. https://doi.org/10.3173/air.26.77

Lekshmi, S. U. S., Singh, D. N., & Baghini, M. S. (2014). A critical review of soil moisture measurement. *Measurement*, *54*, 92–105. https://doi.org/10.1016/j.measurement.2014.04.007

Liu, X., Ren, T., & Horton, R. (2008). Determination of soil bulk density with thermo-time domain reflectometry sensors. *Soil Science Society of America Journal*, *72*(4), 1000–1005. https://doi.org/10.2136/sssaj2007.0332

Lu, S., Ren, T., Gong, Y., & Horton, R. (2007). An improved model for predicting soil thermal conductivity from water content at room temperature. *Soil Science Society of America Journal*, *71*(1), 8–14. https://doi.org/10.2136/sssaj2006.0041

Lungal, M., & Si, B. (2008). Coiled time domain reflectometry matric potential sensor. *Soil Science Society of America Journal*, *72*(5), 1422–1424. https://doi.org/10.2136/sssaj2007.0166N

Malazian, A., Hartsough, P., Kamai, T., Campbell, G., Cobos, D., & Hopmans, J. (2011). Evaluation of MPS-1 soil water potential sensor. *Journal of Hydrology*, *402*(1–2), 126–134. https://doi.org/10.1016/j.jhydrol.2011.03.006

Meng, F., Li, T., Sheng, W., Dixon, C., Zhou, R., & Jones, S. B. (2023). Heat pulse probe design optimization using numerical simulation. *Geoderma*, *436*, 116534. https://doi.org/10.1016/j.geoderma.2023.116534

Menne, D., Hübner, C., Trebbels, D., & Willenbacher, N. (2022). Robust Soil Water Potential Sensor to Optimize Irrigation in Agriculture. *Sensors*, *22*(12), 4465. https://doi.org/10.3390/s22124465

Mori, Y., Hopmans, J., Mortensen, A., & Kluitenberg, G. (2003). Multi-functional heat pulse probe for the simultaneous measurement of soil water content, solute concentration, and heat transport parameters. *Vadose Zone Journal*, *2*(4), 561–571. https://doi.org/10.2113/2.4.561

Mortensen, A. P., Hopmans, J. W., Mori, Y., & Šimůnek, J. (2006). Multi-functional heat pulse probe measurements of coupled vadose zone flow and transport. *Advances in water resources*, *29*(2), 250–267. https://doi.org/10.1016/j.advwatres.2005.03.017

Nagai, T., & Makino, A. (2009). Differences between rice and wheat in temperature responses of photosynthesis and plant growth. *Plant and Cell Physiology*, *50*(4), 744–755. https://doi.org/10.1093/pcp/pcp029

Nissen, H., Moldrup, P., Olesen, T., & Jensen, O. (2001). Time domain reflectometry sensitivity to lateral variations in bulk soil electrical conductivity. *Soil Science Society of America Journal*, *65*(5), 1351–1360. https://doi.org/10.1029/2002WR001303

Nissen, H. H., Ferré, T. P., & Moldrup, P. (2003). Sample area of two-and three-rod time domain reflectometry probes. *Water Resources Research*, *39*(10), 1289. https://doi.org/10.1029/2002WR001303

Noborio, K., Horton, R., & Tan, C. S. (1999). Time domain reflectometry probe for simultaneous measurement of soil matric potential and water content. *Soil Science Society of America Journal*, *63*(6), 1500–1505. https://doi.org/10.2136/sssaj1999.6361500x

Noborio, K., McInnes, K. J., & Heilman, J. L. (1996). Measurements of soil water content, heat capacity, and thermal conductivity with a single TDR probe. *Soil Science*, *161*(1), 22–28. https://doi.org/10.1097/00010694-199601000-00004

Or, D., & Wraith, J. M. (1999). A new soil metric potential sensor based on time domain reflectometry. *Water Resources Research*, *35*(11), 3399–3407. https://doi.org/10.1029/1999wr900226

Peters-Lidard, C., Blackburn, E., Liang, X., & Wood, E. F. (1998). The effect of soil thermal conductivity parameterization on surface energy fluxes and temperatures. *Journal of the Atmospheric Sciences*, *55*(7), 120–1224. https://doi.org/10.1175/1520-0469(1998)055<1209:TEOSTC>2.0.CO;2

Phene, C. J., Hoffman, G. J., & Rawlins, S. L. (1971). Measuring soil matric potential in situ by sensing heat dissipation within a porous body: I. Theory and sensor construction. *Soil Science Society of America Journal*, *35*(1), 27–33. https://doi.org/10.2136/sssaj1971.03615995003500010015x

Philip, J., & Kluitenberg, G. (1999). Errors of dual thermal probes due to soil heterogeneity across a plane interface. *Soil Science Society of America Journal*, *63*(6), 1579–1585.

https://doi.org/10.2136/sssaj1999.6361579x

Rakesh, N., Ahmed, A., Joseph, J., Aouti, R. S., Mogra, M., Kushwaha, A., et al. (2021). Analysis of heat paths in dual-probe-heat-pulse soil-moisture sensors for improved performance. *Sensors and Actuators A: Physical*, *318*, 112520. https://doi.org/10.1016/j.sna.2020.112520

Reece, C. F. (1996). Evaluation of a line heat dissipation sensor for measuring soil matric potential. *Soil Science Society of America Journal*, *60*(4), 1022–1028. https://doi.org/10.2136/sssaj1996.03615995006000040009x

Ren, T., Ju, Z., Gong, Y., & Horton, R. (2005). Comparing heat-pulse and time domain reflectometry soil water contents from thermo-time domain reflectometry probes. *Vadose Zone Journal*, *4*(4), 1080–1086. https://doi.org/10.2136/vzj2004.0139

Ren, T., Noborio, K., & Horton, R. (1999). Measuring soil water content, electrical conductivity, and thermal properties with a thermo-time domain reflectometry probe. *Soil Science Society of America Journal*, *63*(3), 450–457. https://doi.org/10.2136/sssaj1999.03615995006300030005x

Robinson, D. A., Jones, S. B., Wraith, J. M., Or, D., & Friedman, S. P. (2003). A review of advances in dielectric and electrical conductivity measurement in soils using time domain reflectometry. *Vadose zone journal*, *2*(4), 444–475. https://doi.org/10.2113/2.4.444

Saito, H., Šimůnek, J., Hopmans, J. W., & Tuli, A. (2007). Numerical evaluation of alternative heat pulse probe designs and analyses. *Water Resources Research*, *43*(7), W07408. https://doi.org/10.1029/2006WR005320

Saito, H., Šimůnek, J., & Mohanty, B. P. (2006). Numerical analysis of coupled water, vapor, and heat transport in the vadose zone. *Vadose Zone Journal*, *5*(2), 784–800. https://doi.org/10.2136/vzj2006.0007

Scanlon, B. R., Andraski, B. J., & Bilskie, J. (2002), 3.2.4 Miscellaneous methods for measuring matric or water potential, in *Methods of Soil Analysis: Part 4. Physical Methods, Soil Science Society of America. Book Series*. *5*, edited by J. H. Dane, & C. G. Topp, pp. 643–670, Soil Science Society of America, Madison, WI. https://doi.org/10.2136/sssabookser5.4.c23

Woodside, W., & Messmer, J. (1961). Thermal conductivity of porous media. I. Unconsolidated sands. *Journal of applied physics*, *32*(9), 1688–1699. https://doi.org/10.1063/1.1728419

Xin, X., Xu, F., Zhang, J., & Xu, M. (2007). A new resistance sensor for monitoring soil matric potential. *Soil Science Society of America Journal*, *71*(3), 866–871. https://doi.org/10.2136/sssaj2006.0195

Yan, H., He, H., Dyck, M., Jin, H., Li, M., Si, B., et al. (2019). A generalized model for estimating effective soil thermal conductivity based on the Kasubuchi algorithm. *Geoderma*, *353*, 227–242. https://doi.org/10.1016/j.geoderma.2019.06.031

Zhan, T. L., Mu, Q., Chen, Y., & Ke, H. (2015). Evaluation of measurement sensitivity and design improvement for time domain reflectometry penetrometers. *Water Resources Research*, *51*(4), 2994–3006. https://doi.org/10.1002/2014wr016341

Zhang, M., Lu, Y., Heitman, J., Horton, R., & Ren, T. (2017). Temporal changes of soil water retention behavior as affected by wetting and drying following tillage. *Soil Science Society of America Journal*, *81*(6), 1288–1295. https://doi.org/10.2136/sssaj2017.01.0038

Zhang, X., Heitman, J., Horton, R., & Ren, T. (2014). Measuring near-surface soil thermal properties with the heat-pulse method: Correction of ambient temperature and soil–air interface effects. *Soil Science Society of America Journal*, *78*(5), 1575–1583. https://doi.org/10.2136/sssaj2014.01.0014

Zhao, T., Qiao, Z., Zhang, Y., Huang, B., Horton, R., & Liu, G. (2023). Experiments and COMSOL simulations: A comparative study of the heat flux plate method and the gradient method for soil heat flux measurements in barren sand. *Agricultural and Forest Meteorology*, *334*, 109436. https://doi.org/10.1016/j.agrformet.2023.109436